International Journal of Solids and Structures 207 (2020) 230–249

Contents lists available at ScienceDirect

International Journal of Solids and Structures

journal homepage: www.elsevier.com/locate/ijsolstr

Viscous phase-field modeling for chemo-mechanical microstructural evolution: application to geomaterials and pressure solution

A. Guével [a,*], H. Rattez [a], E. Veveakis [a]

[a] Civil and Environmental Engineering Department, Duke University, Durham, NC, USA

ARTICLE INFO

Article history:
Received 3 April 2020
Received in revised form 12 August 2020
Accepted 21 September 2020
Available online 3 October 2020

Keywords:
Phase-field modeling
Contact thermodynamics
Generalized relaxation equation
Geomaterials
Chemo-mechanical
Microstructure
Pressure solution creep
Microstructural viscosity

ABSTRACT

The microstructural geometry of materials has a significant influence on their macroscopic response, especially when the process is essentially microscopic as for chemo-mechanical processes. In this work, we are pursuing the idea that interface-tracking models like phase-field modeling can capture the microstructural dynamics and enrich macroscopic constitutive laws for geomaterials. We are introducing a phase-field theory for chemo-mechanical processes derived from fully-dissipative thermodynamics, enabling the inclusion of dissipative effects such as the evolution of the microstructural curvature. The resulting microstructural viscosity introduces rate-dependency through the associated relaxation time. To emphasize the influence of irregular microstructural geometries, we study numerically the chemo-mechanical response of digitalized geomaterials at the grain scale under pressure solution creep. We show that tracking the grain boundary evolution allows for capturing the microscopic transient nature of pressure solution. Our numerical results are discussed against experimental results from the literature and the properties of macroscopic creep laws are shown to be linked to the evolution of the microstructure.

1. Introduction

1.1. Phase-field modeling

Phase-field modeling (PFM) has been shown to be a framework adequate in modeling interfacial problems. By smoothing the physical sharp interface, it avoids the numerically tedious tracking of the interface. The foundations of PFM date back to van der Waals' use of diffuse interfaces for his capillarity theory in 1893 (Rowlinson, 1979). It is then the works of Landau that paved the way for the phase-field theory. He introduced the Taylor expansion of the system's energy function in the context of phase transitions (Landau, 1937), then the notion of order parameter in his work on superconductivity with Ginzburg (Ginzburg and Landau, 1950), and finally, in 1954 with Khalatnikov (Landau et al., 1965), the time-dependent Ginzburg–Landau equation, called later in the context of PFM the Allen–Cahn equation. Shortly after, Cahn, based on similar ideas but in the context of material sciences (Cahn and Hilliard, 1958), introduced in 1961 the Cahn–Hilliard equation (Cahn, 1961) and with Allen in 1979 the Allen–Cahn equation (Allen and Cahn, 1979), hinging on a variational formulation. The main postulate behind the variational formulation of PFM is that if the free energy is not minimum with respect to a non-conserved order parameter ϕ, then ϕ shall immediately change following the gradient flow equation:

$$\tau\dot{\phi} = -\frac{\delta F}{\delta \phi} \tag{1}$$

with τ the relaxation time to equilibrium and F the free energy functional, yielding the so-called Allen–Cahn equation. An alternative to this variational formulation is the configurational formulation by Fried and Gurtin in 1993 (Fried and Gurtin, 1993), based on the configurational forces theory (Gurtin, 2000) and continuum thermodynamics. While the variational formulation can be checked a posteriori to satisfy the thermodynamic laws, the configurational formulation is derived from them rather than starting from the gradient flow postulate. Firstly, this ensures a clear separation of the balance laws and the constitutive equations (Gurtin, 1996). Secondly, the rate terms need not be a priori prescribed as in the variational formulation (Fried and Gurtin, 1993). Indeed, we recall that PFM is a gradient theory, for the order parameter ϕ but also its gradient $\nabla\phi$ are state variables. The temporal variations of ϕ describe the translations, or normal variations, of the interface, whereas the temporal variations of $\nabla\phi$ (normal vector to the interface) describe the changes of orientation, or tangential variations, of the interface. Those are the two kinematic degrees of freedom necessary to

* Corresponding author.

https://doi.org/10.1016/j.ijsolstr.2020.09.026
0020-7683/

describe the dynamics of an interface, by mathematical definition of a surface. Therefore, omitting the dissipativity of $\nabla\phi$, as usually done in PFM, amounts to assuming that the system is at equilibrium with respect to $\nabla\phi$, or in other words, that the interface can change its orientation without spending energy. In practice, we will see that allowing $\nabla\phi$ to be dissipative induces rate-dependency of the material, as shown in the application to pressure solution. Considering only ϕ to be dissipative yields the usual Allen–Cahn equation, whereas also considering $\nabla\phi$ to be dissipative yields the so-called viscous Allen–Cahn equation. The latter was first derived by Gurtin (1996). We thus argue, from the previous non-equilibrium thermodynamics and interfacial kinematics arguments, that the viscous Allen–Cahn equation offers, in theory, the minimum viable description of a phase field out of equilibrium. An essential difference is that the Allen–Cahn equation is a parabolic equation whereas the viscous Allen–Cahn equation is a pseudoparabolic equation (Ting, 1969). The latter is characterized by a viscous damping of any perturbation, as opposed to an instantaneous dispersion for the former (Barenblatt et al., 1960). We will illustrate numerically the role played by the additional term, the Laplacian rate term, on the kinetics of processes and its relation to the change of interfacial curvature. To obtain a fully-dissipative model while ensuring straightforward coupling of the different processes, we will derive it from a fully-dissipative thermodynamics framework, that we call *contact thermodynamics*, in the form of the *generalized relaxation equation*.

PFM, mostly derived from the variational framework, has been largely applied in material sciences. Notable applications include solid–liquid and solid–solid transitions (Fix, 1983; Langer, 1986; Fried and Gurtin, 1993; Fried and Gurtin, 1994), used in particular to describe crystallographic microstructures such as alloys (Chen and Khachaturyan, 1991; Wang et al., 1993; Zhang and Steinbach, 2012). We point out, in the context of the present study, the PFM of Xu and Meakin (Xu and Meakin, 2008) for dissolution and precipitation, which we will recover to some extent from our non-equilibrium thermodynamics framework. We must also mention the application of PFM to fracture modeling (see Borden et al., 2012 for a thorough numerical treatment and Carlsson and Isaksson, 2020; Dijk et al., 2020 for recent progress), a recent dynamic endeavor that also enriches the panoply of tools available to model geomaterials (see e.g. Heider and Sun, 2020). Another application of PFM to model geomaterials is the tracking of the saturation front in unsaturated media (Cueto-Felgueroso and Juanes, 2009; Sciarra, 2016). We hope to propose here another helpful tool based on PFM to model geomaterials. While the previous tools are concerned with the macroscale, we propose here to track the exact microstructure of geomaterials. The latter cannot be overlooked as the macroscopic dynamics of geomaterials is usually driven from the microscale, as for pressure solution, that we will study in this paper, but also frictional instabilities (Poulet et al., 2014; Rattez et al., 2018; Rattez et al., 2018; Rattez and Veveakis, 2020) and fault reactivation (Veveakis et al., 2014; Lesueur et al., 2020). Unlike discrete-element models, enabling to efficiently describe grains rearrangement (see the topical book O'Sullivan, 2011 and Kawamoto et al., 2018 for recent progress), PFM has received little attention in modeling the microstructure of geomaterials. PFM appears as a promising candidate to capture the highly irregular microstructure of geomaterials in order to better understand their macroscopic behavior, complementarily to discrete-element modeling.

1.2. Pressure solution

The complexity of geomaterials stems mostly from their microstructures, shaped by millions of years of changes of environmental conditions. This renders any geomechanical process unique, all the more since it generally couples different physical processes. There is little choice but explicitly accounting for the geomaterials' microstructures in attempting to fully comprehend their macroscopic response. An archetypal example of such processes is pressure solution, primarily a chemo-mechanical process, and secondarily affected by temperature and hydrodynamics. Pressure solution is microscopically-driven as the microstructural geometry directly controls the strain distribution due to the overburden and, in turn, the strain concentration triggers the dissolution of the grains boundaries.

The concept of pressure solution finds its origin in the realization that the deformation of materials in the presence of fluids cannot be accounted for solely on mechanical bases, but combined with chemical effects. Fluid-bearing materials like geomaterials fall into this consideration. The term "pressure solution" was originally coined by the geologist Sorby, in application to geomaterials, for processes where the "mechanical force is resolved into chemical action" (Sorby et al., 1863). Pressure solution is a major factor in the dynamics of Earth's crust, mainly in the upper crust, as in lithogenesis (Heald, 1956) and tectonics (Schwarz and Stöckhert, 2002). It may also play a significant role in the kinetics of earthquakes via fracture sealing (Renard et al., 2000) and even their onset via pore pressure buildup under densification (Sleep and Blanpied, 1992). A noteworthy observable example of pressure solution creep is the formation of stylolites (see for instance the review paper Toussaint et al., 2018, as well as Gratier et al., 2013). Finally, pressure solution can play a role in underground storage of nuclear waste, both in the case of rock salt cavities (Urai et al., 1986) and bentonite buffers, by making the metallic container sink (Shin, 2017).

Experimental results indicate that diagenesis takes place chiefly by pressure solution rather than by grain straining or crushing (see Lowry, 1956; Renton et al., 1969; de Boer et al., 1977; Schwarz and Stöckhert, 2002 for example). It is thus primordial to take pressure solution into account in the presence of inter-granular fluids, insofar as it can predetermine other processes. Pressure solution creep is a serial stress-driven mass transfer process that can be described in four stages: (1) dissolution at grain impingements, (2) diffusion of the solute out of the contact, (3) deposition/precipitation on the pore surface and potential (4) diffusion/advection of the solute to other pores (see Fig. 1 below adapted from Gundersen et al. (2002)). In the present study, we neglect advective transport, so that the transport of solute is limited to diffusion to nearby pores. The corresponding indicators to look for in experiments are mainly interpenetration and overgrowth. The main drive is mechanical (constant) loading, triggering dissolution in stressed regions and allowing precipitation in sheltered regions relatively understressed (after solute diffusion), first experimentally inferred by Griggs (1940). Since it is an en-serie process, the rate of the slower process will govern the rate of the overall process. Different limiting processes then correspond to different creep laws. A key process is the transfer of mechanical energy into chemical energy throughout the compressed thin layer of trapped fluid between the grains triggering the dissolution. Two main models have been used to explain it: the thin-fluid layer model (Weyl, 1959; Renard et al., 1997) and the island-channel network model (Raj and Chyung, 1981). The main factors influencing pressure solution are the loading stress, the type of minerals, the temperature, the geometry (grain size and porosity inter alia) and the diffusion (and advection if any) coefficients.

To the authors' knowledge, the existing pressure solution studies have suggested two main roadblocks. Firstly, the rate-limiting process (i.e. the slowest process that will control the overall creep law) must be determined on a case-by-case basis, owing to the variety of influencing factors just discussed (Croizé et al., 2013). Therefore, pressure solution creep cannot be described, in general,

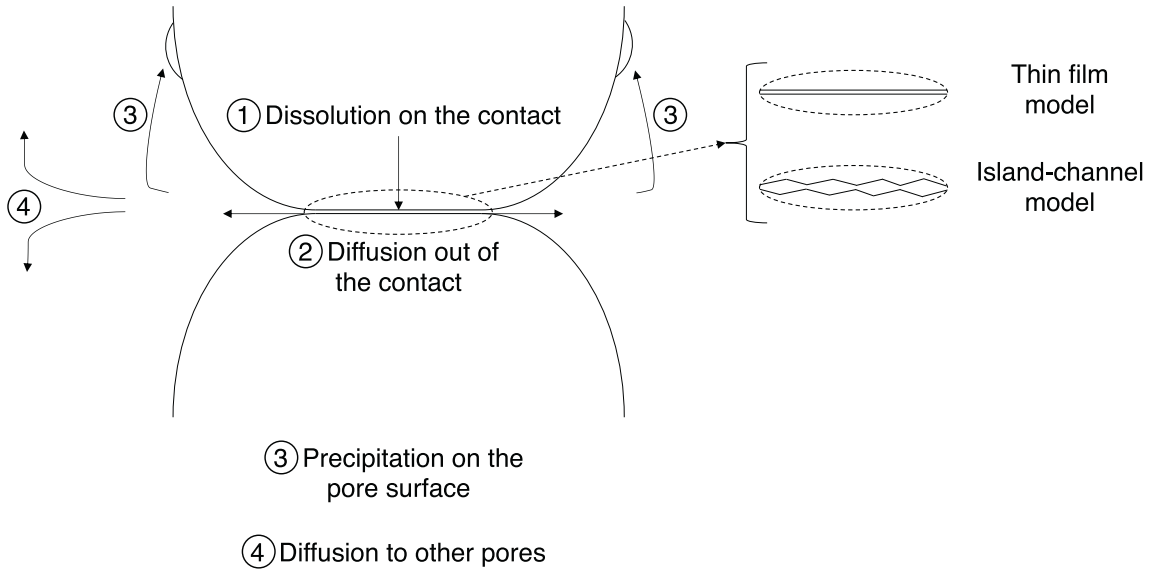

Fig. 1. 4 main processes of pressure solution and 2 main models for grain contacts.

with a unique law (Raj, 1982; Gratier et al., 2013). Secondly, the actual microstructural geometry is typically averaged by regular packs of mono-dispersed spherical particles. This approximation neglects the highly irregular geomaterials' microstructural geometry and its continuous variations during compaction. Even though the grain boundary structures can be approximately taken into account in the creep laws by assuming a thin-film model or islands-channels model, it turns out that the microstrural geometry has a major influence on the compaction rate, in two ways: (1) the compaction rate increases with the grainsize distribution width, i.e. the pressure solution potency increases with the heterogeneity of the microstructure (Niemeijer et al., 2009; Croizé et al., 2013); (2) at high volumetric strains and low porosities, the usual analytical models can overestimate the compaction rates by several orders of magnitude (van den Ende et al., 2019). According to van den Ende et al. (2019), the grain boundary dynamics may be the source of this delay. Indeed, as porosity is reduced, at some point, the grains are interlocked and cannot rearrange without degrading their boundaries, which is not an instantaneous process. Those highly-strained and low-porosity environments are typical of fault gouges and therefore, overlooking the actual microstructure could amount to limiting our understanding of earthquakes nucleation. Accordingly, significant progress has been recently reported in van den Ende et al. (2019) to account for the grain boundary evolution by considering a dynamic island-channel model rather than steady-state. The promising results therein, reconciling existing models with experiments for low porosity, call for further effort in modeling the actual microstructure.

In all, there turns out to be a large consensus that the next step in further understanding pressure solution and its consequences should be modeling the dynamics of the actual geomaterials' microstructure and associated chemo-mechanical microstructural evolution in transient conditions. With the numerical and experimental tools available nowadays, such as large-scale numerical simulations and advanced imaging, it is indeed possible to obtain considerable insights on the microstructural behavior of materials, in particular geomaterials. Indeed, geomaterials digitalization from X-ray computed tomography has paved the way for coupling experimental and numerical insights on the role played by the microstructure (Desrues et al., 1996). On the numerical side, the discrete-element method has largely contributed to this effort (O'Sullivan, 2011; Kawamoto et al., 2018). The idea is not to replace the macroscopic constitutive formulations but rather better constrain them with respect to the microstructures specific to each material. In order to account for grain boundary dynamics, we propose to use phase-field modeling simulations with digitalized microstructures as input. Finally, although the present application is concerned with a microscopic representation of pressure solution, the present model could also accommodate for other microscopic processes such as grain breakage and grain healing. We emphasize that this preliminary study is limited to qualitative results.

2. Viscous phase-field model with chemo-mechanical coupling

2.1. Outlines

Let us first outline the main ideas behind the following derivation (see Fig. 2). We are interested in modeling a microstructure undergoing a chemo-mechanical process. An order parameter ϕ shall differentiate the pores, noted phase A ($\phi = 0$), and the skeleton, noted phase B ($\phi = 1$), subject to elastic mechanical loading. We thereby assume that all irreversible changes of the grains are accounted for by the variations of their interface. The simplest way to approximate the pores phase, assumed fully saturated in liquid, is to model it as a highly deformable shear-free solid, as done for instance in Kassner et al. (2001). Note that it is consistent with the notion of order parameter that its highest value is for the most microscopically "ordered" phase. This mechanical loading, when sufficient, triggers the dissolution of phase B, which resulting solute, of concentration c, can diffuse and precipitate in the phase A, under the appropriate mass balance. The concentration c is introduced as a second phase field for consistency, albeit purely diffusive and thus simply yielding Fick's law. Most importantly, the coupling between the phase field ϕ and the mechanics yields two scales, the microscale for the former and the mesoscale for the latter (see Fig. 2). The mechanics is described by the usual strain tensor $\boldsymbol{\epsilon}$ and the Cauchy stress tensor $\boldsymbol{\sigma}$. For simplicity, we assume small strains. We thus study an assembly of grains subject to the macroforce balance, while each point of this assembly is subject to the microforce balance (acting on the phase-field variables). Such scales separation, inducing two types of force balances, stems from the configurational force theory, complementing the traditional standard force theory in the case

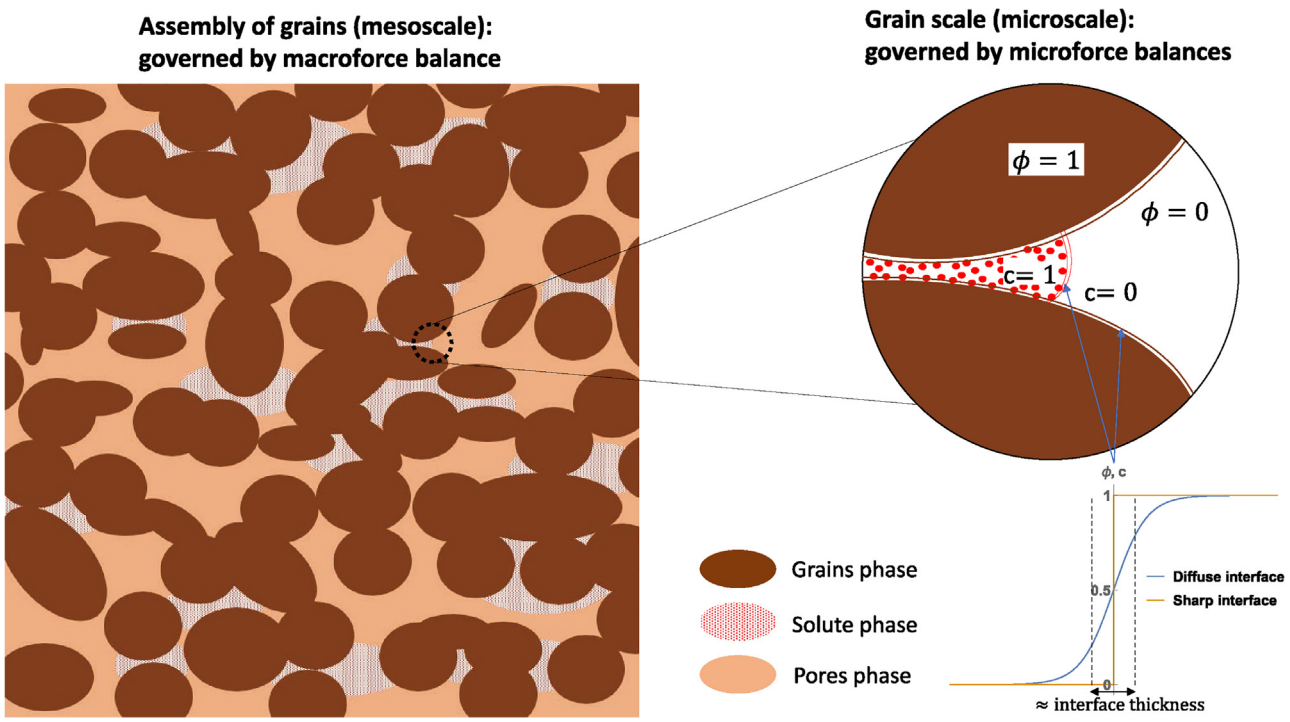

Fig. 2. Sketch of our representation of fully saturated geomaterials' microstructure. The phase-field ϕ differentiates the grains phase ($\phi = 1$) and the pores phase ($\phi = 0$) and the phase field c differentiates in the pores the solute phase ($c = 1$) and the non-solute phase ($c = 0$). The grains are in dark browns, the solute in spotted red, and the pores without solute in light brown. The pores phase is thus the union of the light brown and spotted red phases. On the left, the assembly of grains represents the mesoscale governed by the macroforce balance. On the right, a zoom-in shows the grains scale, i.e. the microscale, where one can distinguish the diffuse interfaces associated to the phase fields ϕ and c. As opposed to the corresponding physical sharp interface, the phase fields progress smoothly from one phase to the other.

of materials with microstructures (see Gurtin, 2000 for a topical review). For the present work, we restrict the problem to isothermal conditions.

Our derivation is threefold. We shall start from the thermodynamic laws and supplement them with the appropriate balance laws and finally complete the specification of the obtained system of equations with constitutive assumptions. We emphasize a clear separation between the fundamental laws and the constitutive postulates, which we summarize in Table 1.

2.2. Thermodynamic foundations

Contact manifold representation Striving to follow a deductive construction of our model, let us start from thermodynamic axioms. Firstly, building on the latest developments in the mathematics of thermodynamics (see Hermann, 1973; Mrugala, 1978; Arnold, 1990; Haslach, 1997 among others), we choose to represent thermodynamic processes in a contact manifold, noted $(\mathscr{M}, \ker\omega)$ (axiom 1). In particular, this representation provides a formal definition of equilibrium. In the general case, should a system be represented by n independent state variables noted in the vector $\boldsymbol{x}$, energetically conjugated with the n control variables $\boldsymbol{y}$ via the free energy ψ, a contact manifold is a smooth manifold $\mathscr{M}$ of dimension $2n+1$ associated with a contact structure $\ker\omega$. We furthermore make the assumption that the free energy $\psi(\boldsymbol{x})$ only depends on $\boldsymbol{x}$ (axiom 2). A contact structure $\ker\omega$ is the kernel of a contact form ω, i.e. a differential 1-form verifying the contact condition:

$$\omega \wedge (\mathrm{d}\omega)^n \neq 0 \tag{2}$$

where d represents the exterior derivative and $\wedge$ the wedge product. This means in particular that the dimension of the submanifold where ω vanishes is at most n (see for instance Geiges, 2008 for a thorough introduction of contact geometry). Such submanifold of maximal dimension n is called a Legendre submanifold. In the context of thermodynamics, the $2n+1$ coordinates $(x_1, \ldots, x_n, y_1,$

Table 1
Summary of the different parts of our viscous PFM with chemo-mechanical coupling, derived from contact thermodynamics. The deductive derivation starts from the fundamental laws, then specified by constitutive assumptions.

Contact thermodynamics	Supplemental balance laws	Constitutive assumptions	
$\boldsymbol{\tau}(\boldsymbol{x},\dot{\boldsymbol{x}}) = \boldsymbol{y} - \frac{\partial\psi}{\partial\dot{\boldsymbol{x}}}$	Microforce balances	State variables $\boldsymbol{x}$	Control variables $\boldsymbol{y}$
(generalized relaxation equation,	Macroforce balance	ϕ	$-\pi_1$
equivalent to dissipation inequality)	Mass balance	$\nabla\phi$	ξ_1
		c	$-\pi_2$
		∇c	ξ_2
		$\boldsymbol{\epsilon}$	$\boldsymbol{\sigma}$
		$\psi(\boldsymbol{x})$ (energy potential)	
		$\boldsymbol{\tau}(\boldsymbol{x},\dot{\boldsymbol{x}})$ (relaxation potential, including dissipation potential $\boldsymbol{\tau}^s$)	

$\ldots, y_n, \psi)$ spanning $\mathscr{M}$ are called the thermodynamic coordinates and ω is called the Gibbs form (Haslach, 1997). As per Darboux's theorem (see e.g. Arnold, 1978 p.362), the Gibbs form can be expressed with respect to the thermodynamic coordinates as:

$$\omega = -\mathrm{d}\psi + \boldsymbol{y} \cdot \mathrm{d}\boldsymbol{x} \tag{3}$$

where "·" represents the scalar product. One can furthermore show that the tangential action of ω reads, for a given tangent vector $\boldsymbol{t}_p$ at any point p of $\mathscr{M}$ (Haslach, 1997):

$$\omega(\boldsymbol{t}_p) = -\dot{\psi} + \boldsymbol{y} \cdot \dot{\boldsymbol{x}} = \boldsymbol{X} \cdot \dot{\boldsymbol{x}} \tag{4}$$

where we introduce the thermodynamic forces vector $\boldsymbol{X} \equiv \boldsymbol{y} - \frac{\partial \psi}{\partial \boldsymbol{x}}$. The superposed dot denotes any infinitesimal increment of time, which should be objective to preserve frame invariance (Truesdell and Toupin, 1960). An example of objective rates is the Lie time derivative, but for simplicity we assume here that the actual configuration of the system coincides with the reference configuration (axiom 3), so that the superposed dot simply denotes the partial derivative with respect to time. We thus adopt a Lagrangian formulation, which in the present chemo-mechanical context, amounts to assuming small strains and neglecting advection.

Now, following 2.1, we choose for our specific problem to represent the system with the following thermodynamic coordinates:

$$\begin{cases} \boldsymbol{x} \equiv (\phi, \nabla\phi, c, \nabla c, \boldsymbol{\epsilon}) \\ \boldsymbol{y} \equiv (-\pi_1, \xi_1, -\pi_2, \xi_2, \boldsymbol{\sigma}) \\ \psi(\boldsymbol{x}) \end{cases} \tag{5}$$

with ψ still to be specified. Adopting the notations of the configurational theory (Fried and Gurtin, 1993; Gurtin, 1996), we remind that π denotes the microforce associated with the phase field and ξ the microstress associated with its gradient (the subscripts 1 and 2 refer to the ϕ and c respectively). To fulfil the laws of thermodynamics, we assume that the system satisfies the second law, in the form of the dissipation inequality (axiom 4). For isothermal conditions and in the presence of configurational forces, the dissipation inequality reads in its local form (see for instance Gurtin, 1996):

$$\mathscr{D} \equiv -\dot{\psi} - \pi_1\dot{\phi} + \xi_1 \cdot \nabla\dot{\phi} - \pi_2\dot{c} + \xi_2 \cdot \nabla\dot{c} + \boldsymbol{\sigma}\dot{\boldsymbol{\epsilon}} = -\dot{\psi} + \boldsymbol{y} \cdot \dot{\boldsymbol{x}} \geqslant 0 \tag{6}$$

where $\mathscr{D}$ denotes the system's local dissipation. Note that even though the energy balance is used to derive the dissipation inequality, it is not considered as a self-standing fundamental law in the present isothermal conditions. The dissipation thus directly relates to the Gibbs form (Eq. 4) as $\mathscr{D} = \omega(\boldsymbol{t}_p)$. The fact that $\mathscr{D}$ can generally be expressed with a 1-form is clearly a motivation underlying the embedment of thermodynamics into contact geometry (Haslach, 1997). Indeed, one can show that conversely, if the dissipation can be written as 1-form with independent functions, it induces a contact structure.

Definition of equilibrium We have now the support to formally define equilibrium. We will say that a system is at equilibrium when $\mathscr{D} = 0$ (axiom 5). According to a theorem due to Arnold (Arnold, 1978 p.367), when ψ is only a function of $\boldsymbol{x}$ (axiom 2), this condition is equivalent to $\boldsymbol{X} = 0$ (but not necessarily $\dot{\boldsymbol{x}} = 0$). Therefore, in the contact manifold $\mathscr{M}$, equilibrium is represented by the Legendre submanifold (of dimension n) generated by the n Legendre equations:

$$y_i = \frac{\partial \psi}{\partial x_i}, \ i = 1, \ldots, n. \tag{7}$$

We remind that this is the space of maximal dimension where the dissipation vanishes. Since we are interested in studying the general case of full non-equilibrium processes, we assume by default that all the components of $\boldsymbol{X}$ are non-zero (axiom 6). If $\boldsymbol{X} \neq 0$ but a certain $X_i = 0$, the system is only partially out of equilibrium. As explained in the next paragraph, we understand full non-equilibrium processes as fully dissipative processes. However, we may relax this axiom a posteriori if observations show that a certain state variable x_i induces negligible dissipation ($X_i = 0$).

General solution of the dissipation inequality The Coleman-Noll procedure shows that in order to have $X_i \neq 0$ (axiom 6), X_i must be a function of $\dot{x}_i$ (Coleman and Noll, 1963). We are thus looking for all the vectors $\dot{\boldsymbol{x}}$ satisfying the following inequality, while considering $\boldsymbol{x}$ as a parameter:

$$\boldsymbol{X}(\boldsymbol{x}, \dot{\boldsymbol{x}}) \cdot \dot{\boldsymbol{x}} \geqslant 0. \tag{8}$$

Following a theorem due to Gurtin (see appendix B of Gurtin, 1996), a necessary and sufficient condition for the system to satisfy the dissipation inequality (8) is that there exist a positive semi-definite tensor $\boldsymbol{\tau}(\boldsymbol{x}, \dot{\boldsymbol{x}})$ such that:

$$\boldsymbol{\tau}(\boldsymbol{x}, \dot{\boldsymbol{x}})\dot{\boldsymbol{x}} = \boldsymbol{X}(\boldsymbol{x}, \dot{\boldsymbol{x}}). \tag{9}$$

Note that a crucial condition for the validity of this solution is that the function $\boldsymbol{X}(\boldsymbol{x}, \cdot)$ be continuous in 0 (axiom 7). We call this tensorial equation the *generalized relaxation equation* and $\boldsymbol{\tau}(\boldsymbol{x}, \dot{\boldsymbol{x}})$ the *relaxation tensor*. Note also that, to be precise, $\boldsymbol{\tau}$ satisfies a condition weaker than positive semi-definiteness since it depends on $\dot{\boldsymbol{x}}$ (Gurtin, 1996). One must specify the relaxation tensor to obtain a system of scalar equations (see 2.4.1) and specify the free energy (see 2.4.2) to obtain an explicit system of equations with respect to $\boldsymbol{x}$ and $\boldsymbol{y}$. The dimension of this system of equations is the thermodynamic degree of freedom, i.e. the number of independent variables by which one chooses to describe the system. This yields a system, in the general case, of n equations with $2n$ unknowns $\{x_1, \ldots, x_n, y_1, \ldots, y_n\}$. In the present example of microstructural chemo-mechanical processes, $n = 5$ (see variables in (5)). This system can be reduced upon applying the relevant balance laws (see 2.3).

We may coin the term *contact thermodynamics* to denote the general framework exposed in 2.2 (axioms and resulting generalized relaxation equation), based on contact geometry. Note that the generalized relaxation equation, although here applied to a special case, holds for any thermodynamic system satisfying the second law of thermodynamics (provided axiom 7). As elaborated in 2.4.1, Edelen (1977) must be acknowledged for proposing the first general solution to the dissipation inequality, although in a dual form to our tensorial formulation.

2.3. Supplemental balance laws

In addition to the thermodynamic laws, equivalent to the generalized relaxation equation, the system's variables are subject to supplemental balance laws. In the present context of chemo-mechanics, and upon neglecting the inertial effects, these are the microforce balance, macroforce balance and mass balance. At the microscale, hold the two microforce balances for the two phase fields ϕ and c (Fried and Gurtin, 1993; Gurtin, 1996):

$$\begin{cases} \nabla.\xi_1 + \pi_1 = 0 \\ \nabla.\xi_2 + \pi_2 = 0. \end{cases} \tag{10}$$

At the mesoscale (with a spatial domain of interest noted Ω), hold the macroforce balance and the mass balance of the reactive species being dissolved and precipitated, present in phase A as solute and in phase B as part of the solid skeleton:

$$\nabla \cdot \boldsymbol{\sigma} = 0, \tag{11}$$

$$\int_\Omega \left(\dot{\phi} + \dot{c}\right) d\Omega = 0. \tag{12}$$

The mass balance here amounts to assuming that the reactive species are either present in a solid form in the skeleton ($\phi = 1$) or in a solute form ($c = 1$).

2.4. Additional constitutive assumptions

All in all, the system is presently described by 8 variables ($\phi, c, \boldsymbol{\epsilon}, \pi_1, \boldsymbol{\xi}_1, \pi_2, \boldsymbol{\xi}_2, \boldsymbol{\sigma}$) and 9 equations (5 scalar relaxation equations from thermodynamics for the 5 state variables and 4 balance equations). The system is therefore over-constrained. This is why the mass balance will be enforced, as often in PFM, as a constraint condition on the system of equations, via a Lagrange multiplier, noted $\beta(\phi)$, in order to satisfy Eq. (12). To fully specify our system of equations, it remains to describe the system's relaxation tensor $\boldsymbol{\tau}(\boldsymbol{x}, \dot{\boldsymbol{x}})$ and its free energy $\psi(\boldsymbol{x})$.

2.4.1. Relaxation tensor

The relaxation tensor $\boldsymbol{\tau}$ describes the time for the system to reach equilibrium with respect to each state variables. Practically, it indicates how the rate terms enter the equations, either dissipatively via its symmetric part $\boldsymbol{\tau}^s$ or non-dissipatively via its anti-symmetric part $\boldsymbol{\tau}^a$ (see App. A). We shall note that it is therefore not sufficient to prescribe, as usually assumed, an energy potential and a dissipation potential, since then the non-dissipative rate terms would be missing. We argue for, instead, using an energy potential and a relaxation potential. Indeed, rate terms can enter an equation without contributing to the dissipation as we will now show for the chemo-mechanical coupling. Edelen has already extensively argued for the incompleteness of a dissipation potential description without taking into account the "gyroscopic" forces (Edelen, 1977; Edelen, 1993), along with Goddard more recently (Goddard, 2014) and Ostoja-Starzewski (Ostoja-Starzewski, 2009; Ostoja-Starzewski, 2014). As pointed out by Goddard, continuum mechanics has a long-standing tradition of using "hyperdissipative" models (such as Ziegler, 1983; Collins and Houlsby, 1997 among many others), meaning that they are fully derived from an energy potential and a dissipation potential, implicitly neglecting the gyroscopic forces (as acknowledged by Ziegler (1983)). Only within such restrictive assumptions exist variational principles such as the maximum entropy production principle. We show in this work that non-dissipative forces are, however, indispensable for chemo-mechanical coupling for instance, and more generally for reaction–diffusion systems, where they play the role of "reactive constraints" (Goddard, 2014) or more practically of source/sink terms. While the latter is usually introduced directly in the diffusion equation (as in Xu and Meakin, 2008), we introduce it as a cross term τ_c of the relaxation tensor. Let us thus define the non-symmetric relaxation tensor in the simplest way as:

$$\boldsymbol{\tau} \equiv \begin{pmatrix} \tau_1 & 0 & 0 & 0 & 0 \\ 0 & \boldsymbol{\tau}_2 & 0 & 0 & 0 \\ \tau_c & 0 & \tau_3 & 0 & 0 \\ 0 & 0 & 0 & \boldsymbol{\tau}_4 & 0 \\ 0 & 0 & 0 & 0 & \boldsymbol{\tau}_5 \end{pmatrix} \tag{13}$$

where $\tau_1, \boldsymbol{\tau}_2, \tau_3, \boldsymbol{\tau}_4, \boldsymbol{\tau}_5$ (all positive quantities) are respectively the relaxation times of $\phi, \nabla\phi, c, \nabla c, \boldsymbol{\epsilon}$. Note that $\boldsymbol{\tau}_2, \boldsymbol{\tau}_4$ and $\boldsymbol{\tau}_5$ are tensors of dimension 3 since they are associated with gradient variables. For simplicity, we assume $\boldsymbol{\tau}_2 = \tau_2 \mathbb{1}, \boldsymbol{\tau}_4 = \tau_4 \mathbb{1}$ and $\boldsymbol{\tau}_5 = \tau_5 \mathbb{1}$, where $\mathbb{1}$ denotes the identity tensor. The scalar τ_c (also positive) is the relaxation time of the chemical coupling, related to the solute propagation. They can depend on any variable x_i but for the present preliminary study we assume the τ_i to be constant. Thereupon, the 5 generalized relaxation equations now read:

$$\begin{cases} \tau_1 \dot{\phi} = -\pi_1 - \frac{\partial \psi}{\partial \phi}, \\ \tau_2 \nabla \dot{\phi} = \boldsymbol{\xi}_1 - \frac{\partial \psi}{\partial \nabla \phi}, \\ \tau_c \dot{\phi} + \tau_3 \dot{c} = -\pi_2 - \frac{\partial \psi}{\partial c}, \\ \tau_4 \nabla \dot{c} = \boldsymbol{\xi}_2 - \frac{\partial \psi}{\partial \nabla c}, \\ \tau_5 \dot{\boldsymbol{\epsilon}} = \boldsymbol{\sigma} - \frac{\partial \psi}{\partial \boldsymbol{\epsilon}}. \end{cases} \tag{14}$$

Note that since we consider the phase field c purely diffusive, i.e. ∇c not dissipative, $\tau_4 = 0$.

2.4.2. Free energy

The free energy acts as an energy potential and describes the system (only) at equilibrium, i.e. its steady states. Indeed, out of equilibrium, the energy potential does not Legendre-conjugate the control variable with its state variable, viz. $X_i \equiv y_i - \frac{\partial \psi}{\partial x_i} \neq 0$. Let us define the following specific free energy for our model (unit: J/m^3):

$$\psi(\phi, \nabla\phi, c, \nabla c, \boldsymbol{\epsilon}) = Gg(\phi) + (1 - h(\phi)) \frac{1}{2} \boldsymbol{\epsilon}.\boldsymbol{C}_A \boldsymbol{\epsilon} + h(\phi) \frac{1}{2} \boldsymbol{\epsilon}.\boldsymbol{C}_B \boldsymbol{\epsilon} + \beta(\phi) c + \frac{\kappa}{2} ||\nabla\phi||^2 + \frac{D}{2} ||\nabla c||^2. \tag{15}$$

The first term is the usual double-well potential with G the double-well's height and $g(\phi) = \phi^2(1-\phi)^2$. The elastic energy (second and third terms) is defined in each phase and interpolated by the interpolation function $h(\phi) = \phi^2(3 - 2\phi)$, with $h(0) = 0$ and $h(1) = 1$. In doing so, we use the Voigt-Taylor homogeneization scheme (Ammar et al., 2009). This consists in interpolating the elastic energies of the different phases, and hence the equilibrium stresses $\boldsymbol{\sigma}_A = \frac{\partial \psi}{\partial \boldsymbol{\epsilon}_A}$ and $\boldsymbol{\sigma}_B = \frac{\partial \psi}{\partial \boldsymbol{\epsilon}_B}$, while assuming homogeneous strain $\boldsymbol{\epsilon}_A = \boldsymbol{\epsilon}_B = \boldsymbol{\epsilon}$. We will see that this hypothesis is coherent with the usual poromechanics formulation. The chemical energy (fourth term) will be determined a posteriori as a Lagrange multiplier to enforce the mass balance. The two last terms are the usual gradient energies for the two phase fields, where κ and D are the associated gradient coefficients. We know from Kim et al. (1999) that the interfacial energy γ [J/m^2] of the interface between the skeleton and the pores scales as $\gamma \sim \sqrt{\kappa G}$ and the corresponding interface thickness l_i [m] as $l_i \sim \sqrt{\frac{\kappa}{G}}$. For the concentration of the solute c, since we assume the particular case where it is purely diffusive, D simply corresponds to the solute's diffusivity.

2.5. Derivation

Let us summarize the different elements of the model in Table 1, emphasizing the distinction between the fundamental laws and the constitutive assumptions. We remind that the system, as such, is over-constrained, and therefore the mass balance is enforced via a Lagrange multiplier. We can combine the 5 generalized relaxation equations (14) with the 3 force balances ($(10)_1$, $(10)_2$, (11)), as well as the prescribed free energy ψ (15), to obtain the 3 evolution equations of ϕ, c and $\boldsymbol{\epsilon}$:

$$\begin{cases} -\tau_2 \triangle \dot{\phi} + \tau_1 \dot{\phi} = \kappa \triangle \phi - f(\phi, c, \boldsymbol{\epsilon}), \\ \tau_3 \dot{c} = D \triangle c - \tau_c \dot{\phi} - \beta(\phi), \\ \nabla \cdot \left(\overline{\boldsymbol{C}}(\phi) \boldsymbol{\epsilon} + \tau_5 \dot{\boldsymbol{\epsilon}} \right) = 0, \end{cases} \tag{16}$$

with $f(\phi, c, \boldsymbol{\epsilon}) \equiv \frac{\partial \psi}{\partial \phi} = Gg'(\phi) + h'(\phi) \frac{1}{2} \boldsymbol{\epsilon}.(\boldsymbol{C}_B - \boldsymbol{C}_A) \boldsymbol{\epsilon} + \beta'(\phi) c$ and $\overline{\boldsymbol{C}}(\phi) \equiv (1 - h(\phi)) \boldsymbol{C}_A + h(\phi) \boldsymbol{C}_B$ the mixed elastic tensor. To enforce

the mass balance (12), we choose $\tau_3 = \tau_c$ and the chemical coupling function to be:

$$\beta(\phi) \equiv \beta\left[1 - h(\phi) - \overline{1 - h(\phi)}\right] \tag{17}$$

where $\overline{1 - h(\phi)} = \frac{\int_\Omega (1-h(\phi))d\Omega}{\int_\Omega d\Omega}$, so that the derivative of β with respect to ϕ is $\beta'(\phi) = -\beta h'(\phi)$. We remind that Ω is the spatial domain of interest.

Note in particular that we obtain the additional Laplacian rate term $\tau_2 \triangle \dot{\phi}$ in the first equation, extending the usual Allen–Cahn equation to the so-called viscous Allen–Cahn equation. It was first introduced by Gurtin (1996) upon assuming the microstress ξ to be dissipative. As previously explained, in our derivation, it stems from allowing the system to be fully dissipative (axiom 6), i.e. out of equilibrium, in particular from allowing $\nabla\phi$ to be dissipative. The second equation is the usual chemical diffusion equation with a (non-dissipative) sink/source term $\tau_c\dot{\phi}$, due to the non-diagonal coefficient of $\boldsymbol{\tau}$. Regarding the third relaxation equation for the mechanics, we emphasize that we recover an interpolation of the partial stresses $\boldsymbol{\sigma}_A$ and $\boldsymbol{\sigma}_B$, consistently with our initial Voigt-Taylor assumption. We have however in addition the viscous term $\tau_5\dot{\boldsymbol{\epsilon}}$ due to assuming $\boldsymbol{\epsilon}$ dissipative. Indeed, the relaxation equation for $\boldsymbol{\epsilon}$ can be written as:

$$\boldsymbol{\sigma} = (1 - h(\phi))\boldsymbol{\sigma}_A + h(\phi)\boldsymbol{\sigma}_B + \tau_5\dot{\boldsymbol{\epsilon}}. \tag{18}$$

We also recover as a particular case, modulo the viscoelastic term and in the case where $h(\phi) = \phi$, the usual mixture of stresses in poromechanics (Coussy, 2004).

The last step of our derivation is to write the previous system in a dimensionless form. Since the terms are homogeneous to a specific energy (or equivalently a stress), we choose our reference specific energy (i.e. reference stress) as the height of the double-well potential G and divide the three equations by G. Note that G directly characterizes the energy required to induce phase change. Then, the reference length is noted l_0 and the reference time t_0, yielding the dimensionless derivatives $\partial^*/\partial t = t_0\partial/\partial t$ and $\triangle^* = l_0^2\triangle$. The dimensionless system thus reads:

$$\begin{cases} -\frac{\tau_2}{Gl_0^2t_0}\triangle^*\frac{\partial^*\phi}{\partial t} + \frac{\tau_1}{Gt_0}\frac{\partial^*\phi}{\partial t} = \frac{\kappa}{Gl_0^2}\triangle^*\phi - f^*(\phi,\boldsymbol{\epsilon},c) \\ \frac{\tau_c}{Gt_0}\frac{\partial^* c}{\partial t} = \frac{D}{Gl_0^2}\triangle^* c - \frac{\tau_c}{Gt_0}\frac{\partial^*\phi}{\partial t} - \beta^*(\phi) \\ \nabla^*\cdot\left(\frac{1}{G}\overline{\boldsymbol{C}}(\phi)\boldsymbol{\epsilon} + \frac{\tau_5}{Gt_0}\frac{\partial^*\boldsymbol{\epsilon}}{\partial t}\right) = 0 \end{cases} \tag{19}$$

Let us fix the reference time scale $t_0 \equiv \frac{\tau_1}{G}$, corresponding to the scaled relaxation time of the normal variations of the interface, but not the reference length scale l_0, which depends on the problem's dimensions. In our case, l_0 will correspond to the characteristic length of the problem's domain Ω. We thereupon define the following dimensionless quantities (see also App. D for a summary of the parameters with their associated numerical values):

$$\begin{aligned} &\mu = \tfrac{\tau_2}{\tau_1 l_0^2}, \\ &\alpha = \tfrac{\kappa}{Gl_0^2}, \\ &f^*(\phi,\boldsymbol{\epsilon},c) = g'(\phi) + \chi(\boldsymbol{\epsilon},c)h'(\phi), \\ &\chi(\boldsymbol{\epsilon},c) = \zeta(\boldsymbol{\epsilon}) - \beta^* c, \\ &\zeta(\boldsymbol{\epsilon}) = \tfrac{1}{2G}\boldsymbol{\epsilon}.(\boldsymbol{C}_B - \boldsymbol{C}_A)\boldsymbol{\epsilon}, \\ &\beta^* = \tfrac{\beta}{G}, \\ &\tau_c^* = \tfrac{\tau_c}{Gt_0}, \\ &D^* = \tfrac{D}{Gl_0^2}, \\ &\beta^*(\phi) = \tfrac{\beta(\phi)}{G}, \\ &\overline{\boldsymbol{C}}^* = \tfrac{1}{G}\overline{\boldsymbol{C}}, \\ &\tau_5^* = \tfrac{\tau_5}{\tau_1}. \end{aligned}$$

For convenience, we drop the $*$ notation and our final system of equations reads:

$$\begin{cases} -\mu\triangle\dot{\phi} + \dot{\phi} = \alpha\triangle\phi - f(\phi,\chi(\boldsymbol{\epsilon},c)) \\ \tau_c\dot{c} = D\triangle c - \tau_c\dot{\phi} - \beta(\phi) \\ \nabla\cdot\left(\overline{\boldsymbol{C}}(\phi)\boldsymbol{\epsilon} + \tau_5\dot{\boldsymbol{\epsilon}}\right) = 0 \end{cases} \tag{20}$$

In particular, the first phase-field equation is characterized by three dimensionless quantities. The dimensionless group $\alpha \equiv \frac{\kappa}{Gl_0^2}$ is the usual phase-field interfacial coefficient. From Kim et al. (1999), we know that α scales as the squared ratio l_i^2/l_0^2 between the interface thickness and the problem's length scale. It is usually recommended that the latter be much bigger than the former, i.e. to have $\alpha \ll 1$ (see for instance Fix, 1983; Aagesen et al., 2017). Otherwise, spurious grain boundary diffusion may occur. Moreover, the smaller α, the closer the problem to the real sharp interface problem. Nevertheless, when α is too small, numerical complications may occur and therefore we shall find a compromise in defining its value in the following numerical simulations. The second dimensionless group $\mu \equiv \frac{\tau_2}{\tau_1 l_0^2}$, that we coin *phase-field viscosity*, appears, to the best of our knowledge, for the first time in the present work. It essentially characterizes the competition between the kinetics of the normal variations of the interface (τ_1) and the kinetics of its tangential variations (τ_2). The third important dimensionless group is the phase-change activation function $\chi(\boldsymbol{\epsilon},c) \equiv \zeta(\boldsymbol{\epsilon}) - \beta c$ containing the different input of energies, here mechanical and chemical, and triggering the phase changes, as detailed in Section 3.1.

2.6. Comparison with existing PFM for dissolution/precipitation

We refer to the model of Xu and Meakin (2008) for a comparison with an existing PFM for dissolution/precipitation (see Eq. 24 and 25 therein). This serves as a valid reference since they prove their equations to converge to the solution of the corresponding sharp-interface problem. They showed that an additional term proportional to the interface curvature should be present in Eq. $(20)_1$ to counteract the curvature-driven interface motion, which may be source of error. Moreover, in Eq. $(20)_2$, they have a different term instead of our term $\beta(\phi)$, accounting for the discontinuity in the solute concentration across the interface. However, there is no direct comparison possible a priori. Indeed, we have an additional mechanical coupling and an additional term $\mu\triangle\dot{\phi}$. The mechanical coupling could be added to the sharp-interface analysis following Kassner et al. (2001) for instance, who thereby modeled surface corrugation instabilites, fundamental in pressure solution for instance. In all, to fully ascertain the physical validity of our phase-field model in the context of pressure solution and capture physical phenomena of interest, we should check the correspondence with the sharp-interface equations. This would also give a more precise physical meaning to all our parameters. The problem's sharp-interface equations may be for instance similar to those derived by Lehner and Bataille (1984) in the context of pressure solution, under the assumption of steady-state compaction creep. If the latter does not hold, Lehner (1995) derived the sharp-interface equations in the case of a regular spheres packing. This is not straightforward and will be the object of future works. In fact, the sharp-interface analysis of the viscous Allen–Cahn equation Eq. $(20)_1$ without any coupling would be a novelty in itself. This would provide a physical meaning for the phase-field viscosity μ.

3. Model's response and parametric study

In this section, we describe first the mechanism of phase transition and, then, numerical simulations considering simple geometries to investigate the role of the different parameters of the system. The system of equations Eq. (20) is implemented and solved numerically using the Multiphysics Object Oriented Simulation Environment (MOOSE[1]), which is a finite-element simulator dedicated to multiphysics nonlinear problems with phase-field capabilities (Gaston et al., 2009; Tonks et al., 2012). Specifically, our model is implemented in the multiphysics module REDBACK (Poulet et al., 2017), which focuses on thermo–hydro-mechanical-chemical processes in geomaterials. To resolve our system of equations, we discretize the problem in space using the finite-element method and in time using a backward Euler scheme, with a Jacobian-Free Newton-Krylov solver.

3.1. Phase-change mechanism and assumptions

In the following numerical examples, we intend to illustrate the roles played by the phase-change activation function $\chi(\boldsymbol{\epsilon}, c) = \zeta(\boldsymbol{\epsilon}) - \beta c = \zeta_B(\boldsymbol{\epsilon}) - \zeta_A(\boldsymbol{\epsilon}) - \beta c$ and the phase-field viscosity μ. The effect of χ is first studied with only the mechanical coupling, i.e. $\chi > 0$ to produce phase A only, and then with chemical coupling, so that χ can take negative values to allow production of phase B. The influence of the dimensionless group α, essentially the ratio of the interface thickness and the problem's characteristic scale, is not emphasized here but we remind from the previous section that one should keep $\alpha \ll 1$ to avoid spurious effects due to interface diffusion. We intend to numerically illustrate that χ plays the role of phase-change trigger, its sign determining which phase is produced, whereas μ controls the kinetics of this phase change, presumably by controlling the change of orientation of the interface. The former is illustrated by displaying phase nucleation in an abstract setting (Section 3.2.1) and the latter by considering geometrical effects (Section 3.2.2).

The (dimensionless) activation function $\chi(\boldsymbol{\epsilon}, c)$ represents the amount of energy input, in our case the difference between the mechanical and chemical energies, at each point in space and time. To visualize its effect, we can write the evolution equation of ϕ far from the interface, i.e. in the limiting case of a zero-thickness interface (where $\alpha \to 0$ and $\mu \to 0$):

$$\dot{\phi} \sim -f(\phi, \boldsymbol{\epsilon}, c) \equiv -g'(\phi) - \chi(\boldsymbol{\epsilon}, c) h'(\phi). \tag{21}$$

Although it is clear that α (scaling as l_i^2/l_0^2) tends toward 0 when l_i does, we make the assumption that μ tends toward 0 with l_i as well, which scaling remains to be assessed. Hence, the evolution of ϕ is essentially dictated by the sign of $f(\phi, \boldsymbol{\epsilon}, c)$, i.e. the sign of $\chi(\boldsymbol{\epsilon}, c)$. More specifically, phase change occurs upon tilting of the double well potential $g(\phi)$, resulting in one phase becoming unstable. This corresponds to a saddle-node bifurcation set on when $|\chi| \geqslant \chi_b$, where χ_b is a certain positive bifurcation value. We can visualize in Fig. 3 the influence of χ on the bulk free energy:

$$\begin{aligned} B(\phi, \boldsymbol{\epsilon}, c) &= g(\phi) + (1 - h(\phi))\zeta_A(\boldsymbol{\epsilon}) + h(\phi)\zeta_B(\boldsymbol{\epsilon}) + \beta\left[1 - h(\phi) - \overline{1 - h(\phi)}\right]c \\ &= g(\phi) + \chi(\boldsymbol{\epsilon}, c)h(\phi) + \zeta_A(\boldsymbol{\epsilon}) + \hat{\beta}(t)c \end{aligned} \tag{22}$$

where $\hat{\beta}(t) \equiv \beta\left(1 - \overline{1 - h(\phi)}\right)$. Since phase A is supposed to be much more deformable than phase B, $\zeta_A(\boldsymbol{\epsilon}) \ll \zeta_B(\boldsymbol{\epsilon})$. Then, as the term $\hat{\beta}(t)c$ is independent from ϕ, it does not influence the way the double well tilts, and we may simply visualize the function

[1] http://mooseframework.org

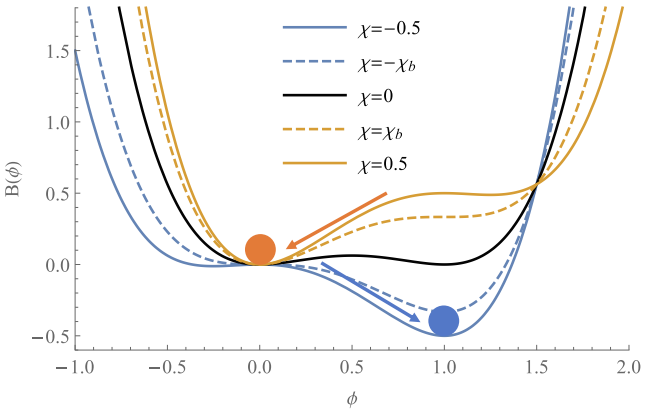

Fig. 3. Graph of the bulk energy $B(\phi, \chi) \approx g(\phi) + \chi h(\phi) = \phi^4 - 2(\chi + 1)\phi^3 + (3\chi + 1)\phi^2$. Upon input of energy, i.e. variations of χ, the double well tilts counter-clockwise when $\chi > 0$, leading to production of phase A at the expanse of phase B (orange curves) and clockwise when $\chi < 0$, leading to production of phase B at the expanse of phase A (blue curves). The phase change (saddle-node bifurcation) happens at $|\chi| = \chi_b$ (dashed curves).

$B(\phi, \chi) \approx g(\phi) + \chi h(\phi)$. In the present context of pressure solution, the production of phase A (orange curves in Fig. 3) corresponds to dissolution and the production of phase B (blue curves in Fig. 3)) to precipitation.

We will consider in the following of this paper a 2D geometry in (x, y) plane strain for simplicity and to show qualitatively the behavior of the model. However, the model has been also implemented in a 3D numerical framework to provide quantitative results that will be the focus of future studies. The elastic energy for phase A and phase B now simply reads:

$$\begin{cases} \zeta_A(\boldsymbol{\epsilon}) = \frac{1}{2}\lambda_A\left({\epsilon_{xx}}^2 + \epsilon_{yy}^2\right), \\ \zeta_B(\boldsymbol{\epsilon}) = \frac{1}{2}\lambda_B\left({\epsilon_{xx}}^2 + \epsilon_{yy}^2\right) + \mu_B\left({\epsilon_{xx}}^2 + \epsilon_{yy}^2 + 2\epsilon_{xy}^2\right), \end{cases} \tag{23}$$

with λ_K and μ_K the Lamé parameters of phase K. We remind that phase A is considered as a shear-free solid with much lower stiffness than phase B, so that $\mu_A = 0$ and $\lambda_A \ll \lambda_B$. Furthermore, we assume that the mechanical equilibrium (at the mesoscale) for $\boldsymbol{\epsilon}$ is reached much faster than the equilibrium of ϕ and c, so that $\tau_5 = 0$. Then, it is sensible to assume that the solute diffuses faster than the microstructure rearranges, i.e. c relaxes faster than ϕ, so that $D \gg \alpha$, which is easily satisfied as $\alpha \ll 1$. Note that different reaction diffusivities are characteristic of such reaction–diffusion systems.

In all our numerical studies, we will work with the following consistent units system: length in *mm*, mass in *kg*, time in *ks*, energy in *J*, pressure/stress in *GPa*. We scale the specific energies and stresses by fixing $G = 1$ GPa. We choose $\tau_1 = 1$ GPa.ks, so that the characteristic time scale is $t_0 = 1$ ks. Those values will be kept in all simulations. As of α, Ghoussoub and Leroy (2001) indicates for instance for a typical silica/water interfacial energy a value of 0.1 Pa.m, i.e. $\gamma_{sf} = 10^{-7}$ GPa.mm. Since α scales like $\frac{\gamma^2}{G^2 l_0^2}$, then $\alpha \sim 10^{-14}$, as our problem's scale will be of the *mm* order. This is consistent with our recommendation $\alpha \ll 1$ to avoid spurious interface diffusion. However, values of α too small (typically in our case for $\alpha < 0.01$), can alter the numerical performance, such as convergence. Hence in practice, as usual in PFM, α is taken as small as numerics allows (Aagesen et al., 2017). Regarding the mechanical properties, we consider the pores phase A saturated with water (brine), under our shear-free solid assumption, and then $\lambda_A \approx 1$ GPa (water's bulk modulus). Although we are interested in modeling sands or sandstones, as an example, their

mechanical characteristics would be valid for phases A and B altogether as a mix but not for phase B alone. We thus consider the pure skeleton phase as a rock with very low porosity, like granite. Hence we choose $\lambda_B \approx 30$ GPa and $\mu_B \approx 30$ GPa, which are values close to what can be found in the literature (Detournay and Cheng, 1993). Note that all numerical parameters are gathered in App. D.

To characterize the output, we choose to define the interface as $\phi \in [0.21, 0.79]$, corresponding to the inflection points of the double well at rest, also called spinodal interval (Cahn, 1961). Then the pure phases A and B are respectively defined by $\phi \in [0, 0.21]$ and $\phi \in [0.79, 1]$. Note that the three regions, pure phase A, interface and pure phase B, are intentionally defined to overlap (in $\phi = 0.21$ and $\phi = 0.79$), which corresponds to the matching condition in a matched asymptotic analysis (see Fried, 2006 for example). The main output we are interested in is the mechanical response of the granular assembly, viz. the stress averaged on the top boundary (dimensionless) versus the vertical strain (in %).

3.2. Parametric study

In the following sections, we present the results of problems chosen to showcase the effect of the main parameters (χ and μ) controlling the mechanical response of the system.

3.2.1. Effect of the phase-change activation function when $\chi > 0$

We investigate first the numerical response of the system considering only mechanically-induced dissolution to study the role of the dissolution activation function, when χ is only a function of $\boldsymbol{\epsilon}$, viz. $\chi(\boldsymbol{\epsilon}) = \zeta_B(\boldsymbol{\epsilon}) - \zeta_A(\boldsymbol{\epsilon})$ (orange curves in Fig. 3). To display the nucleation of phase A in a square domain under mechanical loading, we consider the extreme case where there is initially no phase A, with initial conditions randomly fluctuating in the phase B, i.e. $\phi \in [0.79, 1]$. The boundary conditions are those of an biaxial compression, that is, constantly moving boundaries towards the center (dimensionless velocity of 1), and null Neumann conditions for the order parameter. Note that the latter boundary condition will be satisfied for all the following simulations. The phase field ϕ can be visualized in Fig. 4 at the initial, nucleation of the phase change (corresponding to the peak stress) and final stages of our simulation. Associated is the stress/strain response for two different stiffnesses. The nucleation of the weak phase A, the pores, stemming from the initial fluctuations, leads to a mechanical softening of the material. At a same vertical strain, the stiffer the material, the larger the amount of elastic energy accumulated in the structure, the larger the activation χ and therefore the smaller the deformation to trigger the phase change. Note that the numerical results here hardly bear any physical meaning but simply display the qualitative effect of χ in a simple setting.

3.2.2. Effect of the phase-field viscosity μ

First of all, we may corroborate the viscous effect of the Laplacian rate term $\mu\triangle\dot{\phi}$ by solving numerically the viscous Allen–Cahn equation in the simplest case, without coupling and in 1D (see App. B). As expected for a pseudoparabolic equation, the viscous coefficient μ delays the convergence to the steady states, i.e. the phase change. Then, to more practically highlight the influence of μ, we perform a displacement-controlled oedometric compression of a square including one spherical pore. This geometry enables to have a constant initial curvature of the interface without involving the effect of grains interaction, focus of the next example. More specifically, we aim at illustrating our postulate that the Laplacian rate term induces a viscous effect (proven in App. B) by delaying the variations of the interfaces curvatures, or more exactly the change of interfaces orientation (see App. C). A constant velocity is applied on the top boundary. Unlike previously in 3.2.1, this simple simulation may bear physical meaning, namely pore collapse.

To start with, we perform a mesh convergence study upon the peak stress, for $\mu = 1$, visualized in Fig. 5 with the peak stress values for different mesh resolutions. We may thus use a mesh of dimension (at least) 100×100 elements. The output of the compression (Fig. 6) is then shown for different values of μ right after the onset of softening, i.e. just after the stress has peaked. The softening of this structure translates geometrically into a collapse of the circular pore. As expected, the higher μ, the more delayed the softening response. This effect is clearly achieved by reducing the change of interface curvature, via the Laplacian rate term $\triangle\dot{\phi}$. We remind that the presence of this term is due to the fact that $\nabla\phi$ is allowed to be dissipative in our model. Without this term ($\mu = 0$), the change of curvature is quasi-instantaneous, from a constant curvature to a very large curvature, resulting in a loss of smoothness of the interface and leaving horizontally-flat indentations on the sides. Furthermore, it is important to stress that increasing μ not only delays the response in time (horizontal translation of the curves in Fig. 6), but also induces a vertical translation resulting in a different peak stress. We can thus draw two preliminary insights about the effect of the phase-field viscosity μ. Firstly, at the microscale, the associated Laplacian rate term seems to control the interface curvature and mitigate the apparition of infinite interface curvature. Recall that the curvature dynamics is central to PFM since the Laplacian of the order parameter $\triangle\phi$ measures essentially the curvature of the interface, or at least its change of orientation (see App. C). In that sense, $\triangle\dot{\phi}$ acts as a viscous damping for the change of curvature. Secondly, more than delaying the kinetics of the process, at the mesoscale μ increases the material's resistance to softening (corroborated for a geomaterial's microstructure in Fig. 9), while the static mechanical properties remain the same. The phase-field viscosity μ, when modeling microstructures, can thus be seen as a microstructural viscosity.

Finally, the present diffuse-interface simulation of pore collapse should be related, in the context of pressure solution, to the sharp-interface study of Ghoussoub and Leroy (2001). Similarly, after a slow "ovalization", a rapid lateral dissolution occurs following the stress concentration in a crack-like pattern. However, while the velocity of the crack tip tends to infinity quasi-instantaneously upon crack nucleation in the sharp interface model (see Fig. 8 in Ghoussoub and Leroy (2001) e.g.), the phase-field viscosity μ enables to control the velocity of the lateral openings, via penalization by the Laplacian rate term of the change of curvature.

3.2.3. Effect of the precipitation activation coefficient β (when χ can also be negative)

We now turn our attention to the full chemo-mechanical coupling (i.e. considering both dissolution, when $\chi > 0$, and precipitation, when $\chi < 0$), and in particular the term βc in Eq. $(20)_1$ that triggers the production of the strong phase B ($\phi = 1$). As explained previously, this term allows $f(\phi, \boldsymbol{\epsilon}, c)$ to become negative and hence $\dot{\phi}$ to become positive (blue curves in Fig. (3)). To highlight the processes taking place during pressure solution, we assess the influence of this term and benchmark the validity of the physical mechanisms of our approach against existing theoretical and phenomenological studies on pressure solution (in particular Weyl, 1959), in the case of a simple contact problem. The initial setup leading to the simulation results in Fig. 7 consists of two half-circles representing two grains separated by a thin layer of pores "fluid" under a constant stress of 200MPa and oedometric conditions. We assume that the diameter of those idealized grains is 300 μm so that we choose $l_0 = 0.3mm$. The parameters of the diffusion equation Eq. $(20)_2$ are chosen so that $\tau_c = 1$ and $D = 10$. We

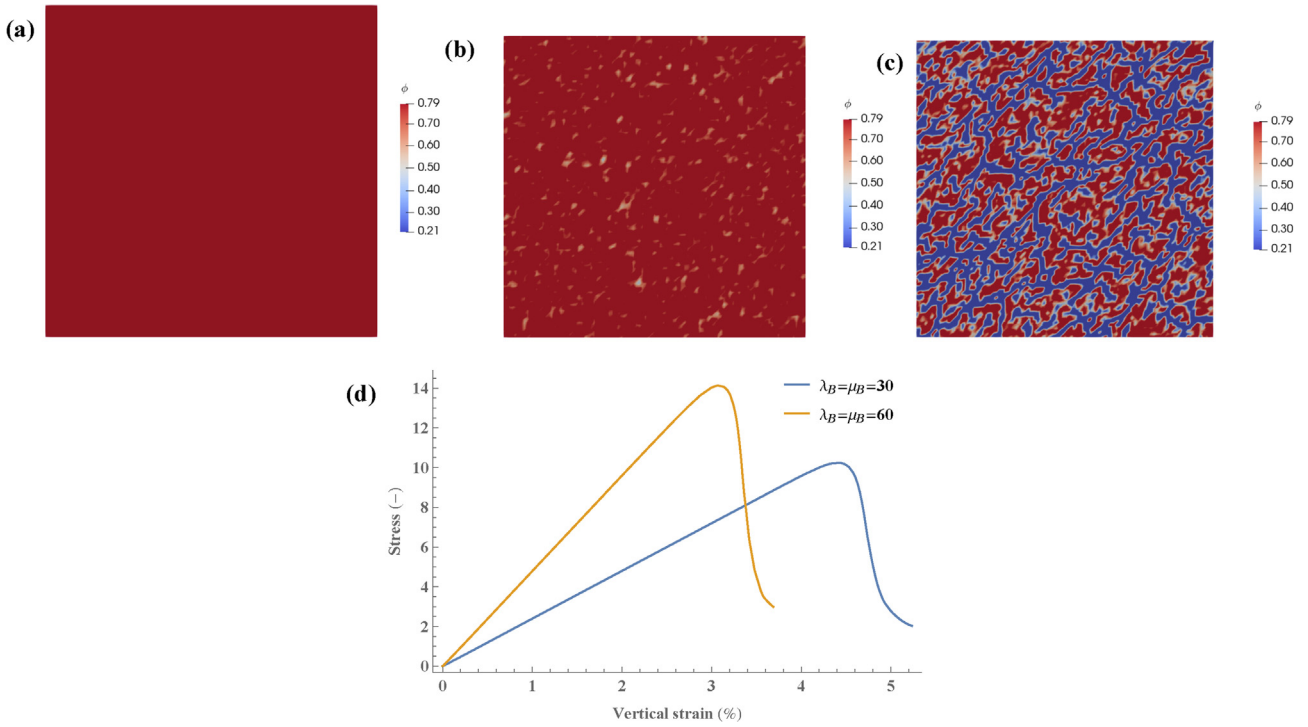

Fig. 4. Nucleation of phase A ($\phi = 0$) under isotropic compression with a mesh of 100×100 triangular elements. The phase-field evolution is shown for $\lambda_A = 1, \mu_A = 0, \lambda_B = \mu_B = 30$ at (a) initial time, (b) onset of softening ($vs = 4.48\%$) and (c) final time ($vs = 5.23\%$). (d) The stress/strain response (averaged on top boundary) is shown for two different stiffnesses. Note that this is an abstract setting to illustrate the effect of χ and does not correspond to any particular physical situation.

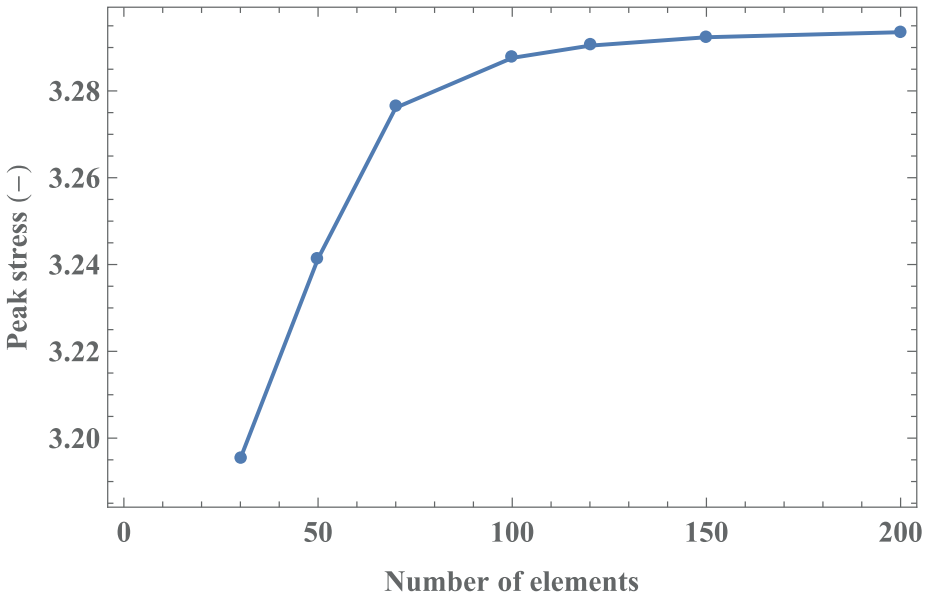

Fig. 5. Mesh convergence study with respect to the peak stress value. We estimate that the mesh is converged for a mesh of at least 100×100 elements.

will assume for all the simulations involving the solute concentration an initial condition $c = 0$. The choice of β is more sensitive as it directly controls the phase change. Upon performing simulations for different values of β, one can show that the higher its value, the later the failure time (jump in vertical strain in Fig. 7). This seems due to the fact that β (linearly) controls the precipitation potential βc, which leads to the precipitation of the dissolved material, thus delaying the overall compaction. In practice, we choose $\beta = 0.05$ so that it has a noticeable effect compared with the case without precipitation. Our pressure solution model for the ideal case of two grains displays two clear stages (see Fig. 7): (1) the dissolution of the high-strain zone, and (2) "contact" between the two flattened grains. The rounded grains' surfaces are dissolved at the contact zone from the sides towards the center until they become flat and there is no more support for the upper grain. Then a failure phase is characterized by a sudden increase in vertical displacement and the two flattened grains come into "contact", still separated by a thin layer of fluid. Successive dissolution stages can be triggered on the flattened surfaces should the system be given enough energy (i.e. time in the present case of constant loading). Coupled with the dissolution, the precipitation of the solute occurs on the sides of the grains (see precipitation rate in

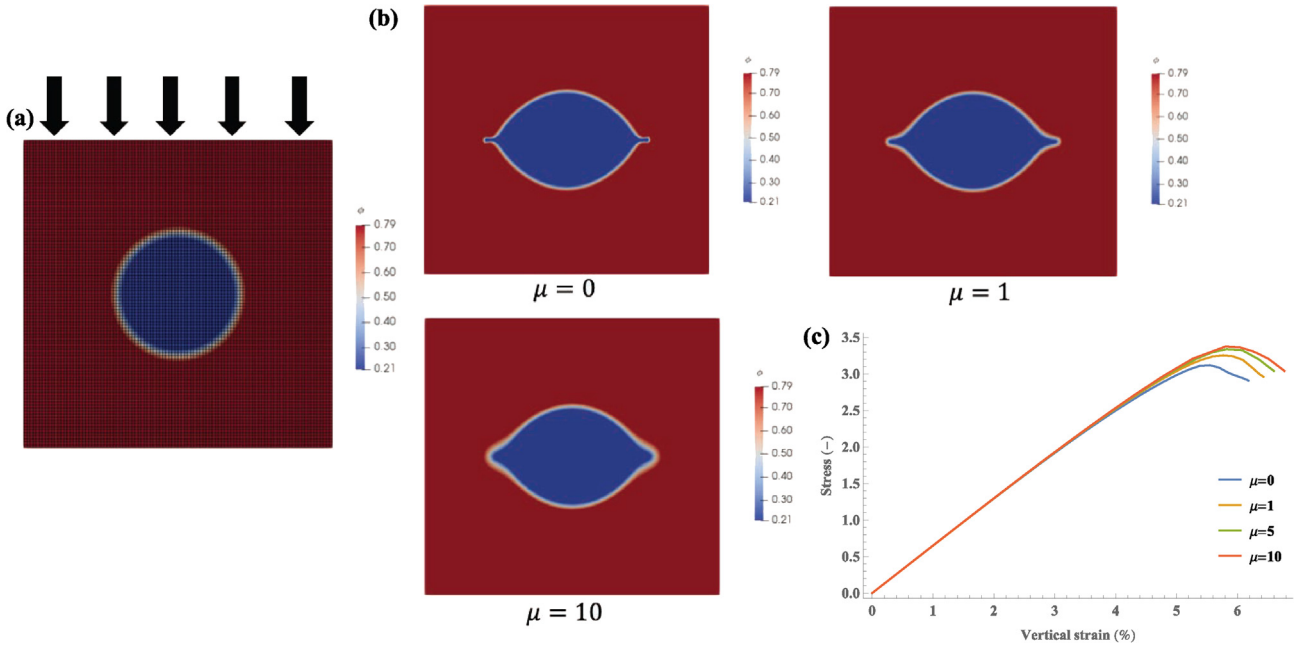

Fig. 6. Oedometric compression of a circle inclusion of weak phase (blue). The phase-field evolution is shown from (a) initial condition to (b) right after onset of softening for different values of μ. (c) The associated stress/strain curves exhibit a top-right translation with increasing μ.

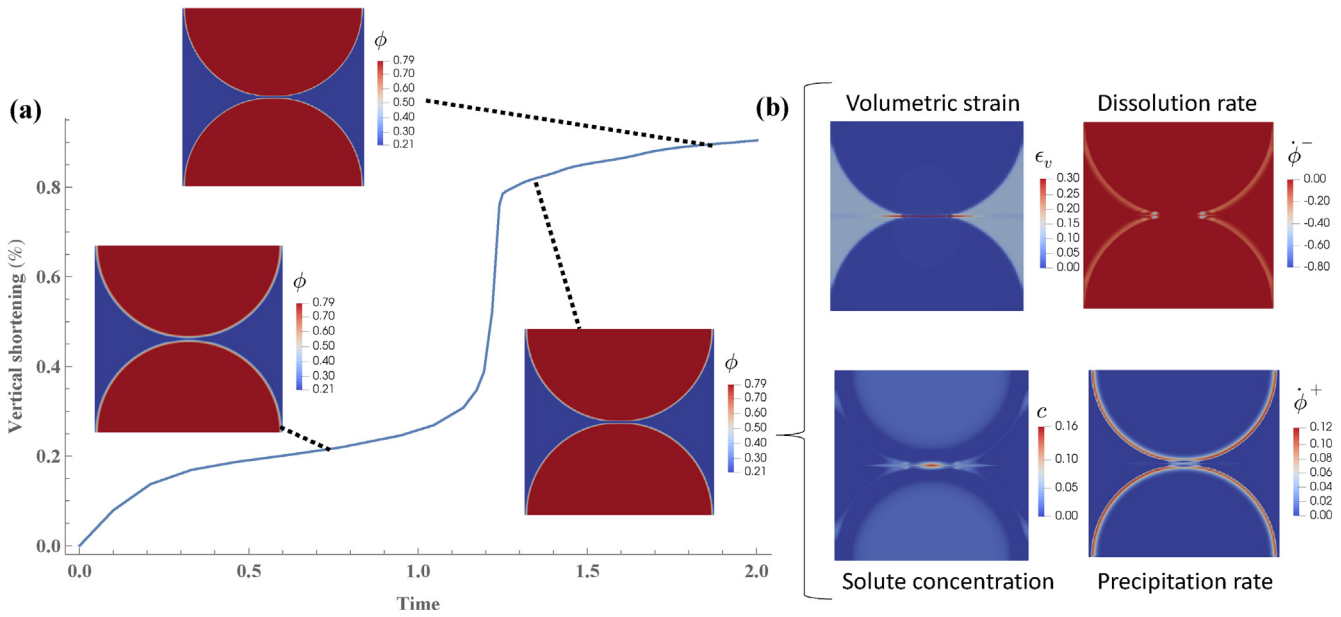

Fig. 7. Pressure solution creep of a two-grain assembly with a mesh of 100 × 100 quadrilateral elements. (a) The vertical strain response can be seen as a tertiary creep, with an initial elastic loading (until $t \approx 0.2$) followed by a primary creep and a secondary creep (between $t \approx 0.4$ and $t \approx 1.1$). We show the phase field during secondary creep at $t = 0.77$. This stage with little displacement displays the dissolution of the grains boundary at the contact, getting undercut and flattened, leading to a sharp increase in displacement. This is characteristic of a tertiary creep. We show the phase field at the end of the tertiary creep at $t = 1.32$. Finally, a second stage of secondary creep may occur, along with undercutting from the sides. We show the phase field during this new secondary creep at $t = 1.88$. (b) On the right are displayed, at $t = 1.32$, the volumetric strain ϵ_v, concentrated at the contact, leading to dissolution (negative part of $\dot{\phi}$), production of solute of concentration c and precipitation of this solute on the sides of the grains (positive part of $\dot{\phi}$).

Fig. 7). This sequence is in accordance with theoretical and phenomenological approaches on the mechanisms of pressure solution (Weyl, 1959). More specifically, the present numerical results illustrate the so-called marginal dissolution, or undercutting, constitutively accounted for in the dynamic island-channel model of van den Ende et al. (2019). Furthermore, the results illustrate the basic process underlying tertiary creep. This simple case also exemplifies why α should be small enough to avoid spurious grain boundary diffusion and subsequent grains merging during the compression.

4. Numerical study of chemo-mechanical microstructural evolution in geomaterials: example of pressure solution

After benchmarking the different features of our model, we apply it to more realistic microstructures, those of geomaterials.

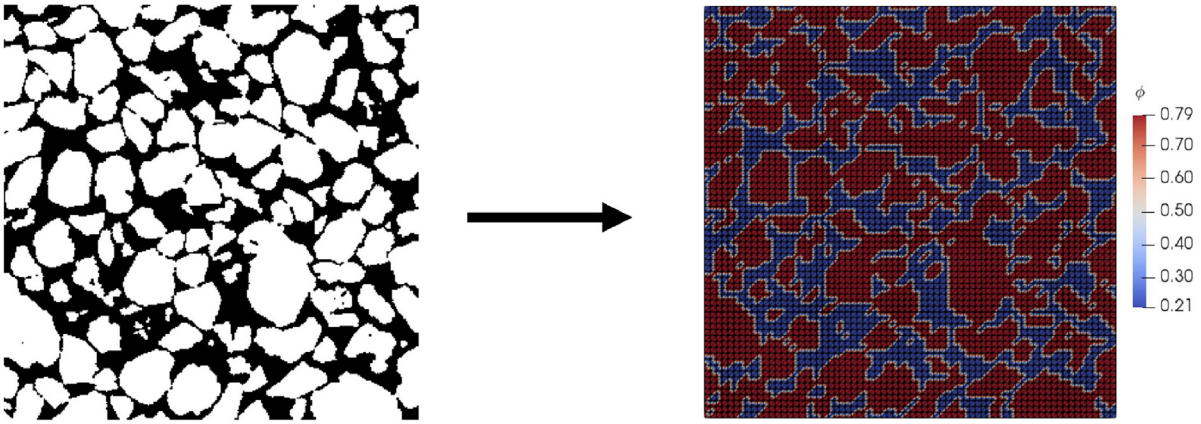

Fig. 8. Digitalization of a LV60A sandpack's CT-scan obtained from Dong and Blunt (2009).

We use as input digitalized CT-scan images of a sandpack obtained from Dong and Blunt (2009) and accessible online[2]. Unless mentioned otherwise, we use the layer number 159 therein.

4.1. Digital modeling of geomaterials

The initial conditions are obtained by digitalizing the segmented image from the CT-scan (Fig. 8). We use a 70×70 mesh for an initial CT-scan whose pixel resolution is 300×300. Obviously, to preserve the resolution, we should use a mesh of 300×300, but this is unnecessarily computationally expensive for the present qualitative study. The dimensions of the CT-scan image are 3×3 mm^2. Therefore, the reference length for the CT-scan simulations is chosen as $l_0 = 3$ mm. Note that the average grain size is 0.3 mm and the particle size distribution is fairly uniform (Talabi et al., 2009).

We start by showcasing the main capabilities of our model applied to a geomaterial's microstructure considering the mechanically-induced dissolution only. The geometry shown in Fig. 8 is oedometrically compressed (applying constant velocity) from the top under varying values of μ. The mechanical response is plotted similarly to the previous simulations (Fig. 9), along with the mean stress and strain distributions, as well as the phase field for different μ at a same given time. The distribution of the mechanical loading from the top boundary throughout the microstructure is clearly displayed by chain-forces-like patterns for the mean stress and by concentration bands for the strain. One can also ascertain that μ indeed controls the onset of softening (lateral translation of the graph in Fig. 9) and the value of the corresponding peak stress (vertical translation of the graph). The phase-field viscosity can thus be seen as microstructural viscosity inducing a rate-dependent behavior of the material, as already discussed in 3.2.2. We can visually assess in Fig. 9 that this results from the decrease of deformability of the interfaces with increasing μ: at a given time, the grains appear more "mixed" for low μ, suggesting that dissolution of the grains in the fluid is promoted for low values of μ. On the other hand, high values of μ tend to delay dissolution and therefore preserve the shape of the microstructure.

4.2. Application to pressure solution creep

Next we apply our model to pressure solution by also allowing for precipitation to take place, and oedometrically applying a constant stress on sections of the sandpack's CT-scan from Dong and Blunt (2009). The constant stress loading is applied smoothly with a hyperbolic tangent function (see App. D). Since we are studying a sandpack composed of quartz grains, the pressure solution reaction corresponds to the dissolution/precipitation reaction of silica ($SiO_{2(s)} + 2H_2O_{(l)} \rightleftharpoons Si(OH)_{4(aq)}$). Thus the skeleton phase is silica, the pore phase is water (brine) and the solute (of concentration c) is silicic acid. Although we are only interested in the present study in qualitative estimation, one may use, for a precise quantitative study, the relevant chemical properties to determine the chemical parameters β, τ_c and D.

4.2.1. Chemo-mechanical response

As expected from the model's equations and the double-well mechanism (Fig. 3), dissolution should happen in high-strain zones (so that $\chi(\epsilon, c) > \chi_b$) and conversely precipitation should happen in low-strain zones (so that $\chi(\epsilon, c) < -\chi_b$). We illustrate numerically in Fig. 10 the pressure solution process for CT-scan #159 at $t = 8.1$ at the end of a major phase change, namely the dissolution of a supporting bridge in the center of the granular assembly inducing a jump in vertical strain (see green curve in Fig. 11). The volumetric strain output (Fig. 10(b)) shows the strain concentration bands where dissolution is favored, producing solute of concentration c (Fig. 10(c)) that can diffuse to sheltered pores with less mechanical energy to precipitate (Fig. 10(d)). Dissolution is checked to consistently affect mainly sharp edges and bridges, i.e. the parts of the grains with the highest ratios surface available to dissolution over internal volume.

4.2.2. Influence of the microstructure's geometry

Since pressure solution is clearly determined by the strain distribution, we expect to have a different response for different initial geometries. We show in Fig. 11 the vertical strain response of different CT-scan layers from the same sand pack from (Dong and Blunt, 2009), including the one used so far (#159). This confirms that while keeping all the material characteristics constant, different microstructures induce different mechanical responses. In particular, different dissolution events induce different jumps in the vertical strain responses. Those jumps, due to microstructural rearrangement, are characteristic of a non-steady state response and appear to corroborate the general consensus that pressure solution is a transient process (Renard et al., 2001; Dysthe et al., 2002; van den Ende et al., 2019). Nonetheless, all the different microstructures seem to follow a general trend already pointed out by Dysthe et al. (2002). Therein, it is claimed from creep experiments on halite and microscopic modeling that geomaterials' response to pressure solution creep follows a power law to the cubic root of time, similarly to transient creep in metals (Andrade, 1910). Interestingly, we indeed obtain in Fig. 11 the so-

[2] https://www.imperial.ac.uk/earth-science/research/research-groups/perm/research/pore-scale-modelling/micro-ct-images-and-networks/sand-pack-lv60a

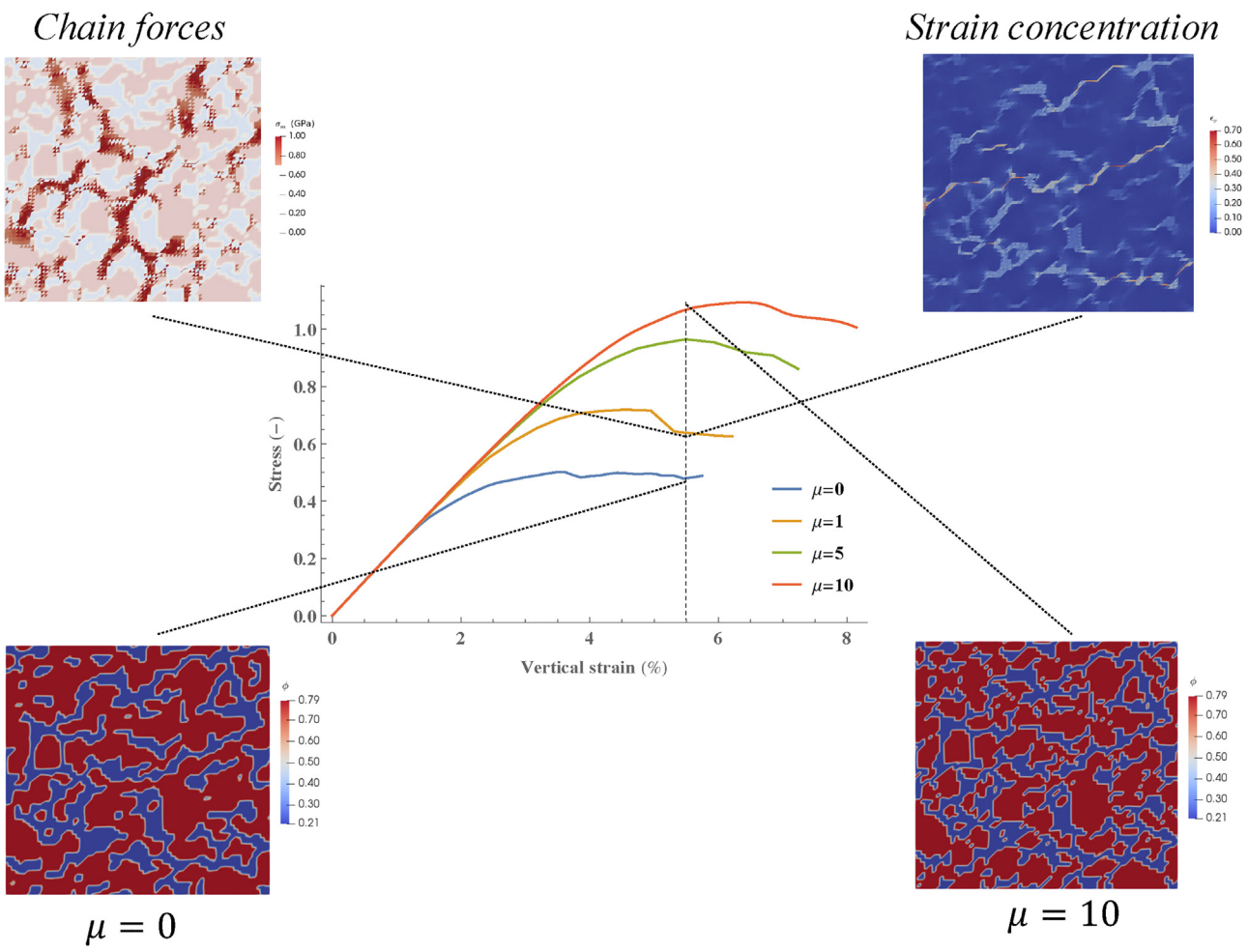

Fig. 9. Simulations outputs for CT-scan simulations under constant-velocity loading for a same vertical strain ($\epsilon = 5.5\%$) for different values of μ and associated stress/vertical strain curves. While our model captures the characteristic features of chaine-force distribution and strain concentration bands, the phase-field viscosity μ introduces a new feature, the control of the rate-dependency, e.g. here the peak stress and onset of softening.

called Andrade creep responses for the different microstructures, namely the vertical strain follows $\epsilon \sim kt^{1/3}$, with k the compaction rate differing for each microstructure. To prove it, we show in Fig. 12 the logarithmic response of the different CT-scan layers, associated with the experimental data obtained from Dysthe et al. (2002). As discussed in Dysthe et al. (2002), the compaction rate parameter k (i.e. y-intercept in Fig. 12(a)) is observed to depend on the microstructure.

4.2.3. Effect of the phase-field viscosity in the context of pressure solution

As showcased previously, μ represents the phase-field viscosity, controlling the kinetics of the phase change regardless of the responsible catalytic sub-processes at stake. The diverse catalytic effects thus need not be explicitly accounted for, as they can be encapsulated altogether in μ. For that, one can associate with each catalytic process an activation energy Q_i and use for instance an Arrhenius law $\mu = \sum_i A_i \left(1 - e^{-\frac{Q_i}{k_B T}}\right)$, where A_i is the pre-exponential factor, k_B is Boltzmann's constant and T the (constant) environmental temperature. In the case of pressure solution, two main such effects reported in the literature can be the temperature (Niemeijer et al., 2002) and the presence of clays (Renard et al., 2001), both experimentally shown to enhance the process when they increase.

Let us consider first the case of clay-enhanced pressure solution. Renard et al. (2001) have experimentally shown that pressure solution is more potent on aggregates of brine-saturated halite and clay, as compared with brine-saturated halite. It is reported therein that the clay particles present at the interstice between the grains of salt may mechanically enhanced pressure solution. Beyond the exact physical reason behind clay-enhanced pressure solution, it is clear that clay particles increase the compaction rates. Renard et al. (2001) also reported experiments on brine-saturated halite with silicate with similar catalytic characteristics. We qualitatively show in Fig. 13 that a decrease of μ also increases the compaction rate. For that, we visualize the logarithmic response showing again an Andrade creep (Fig. 13(c)). Namely, a decrease of μ, while preserving the Andrade creep response (line of slope 1/3), leads to a top-left translation of the curve, i.e. a change of compaction rates. For comparison, we have reproduced in Fig. 13(d) the experimental results from Renard et al. (2001) also in logarithmic values. One can relate a slower response, due to higher μ, to a slower microstructural kinetics. Indeed, the jump previously pointed out at $t = 7.5$ due to the dissolution of a supporting bridge, appears later for higher μ ($t = 11.5$ for $\mu = 0.5$ and $t = 15$ for $\mu = 1$). One could for instance associate the brine experiment (black curve in Fig. 13(d)) with $\mu = 1$ (green curve in Fig. 13 (c)), the silicate experiment (dark gray curve in Fig. 13 (d)) with $\mu = 0.5$ (orange curve in Fig. 13 (c)) and the clay experiment (light gray curve in Fig. 13 (d)) with $\mu = 0$ (blue curve in Fig. 13 (c)). A quantitative matching with experiments would require to prescribe the different parameters of

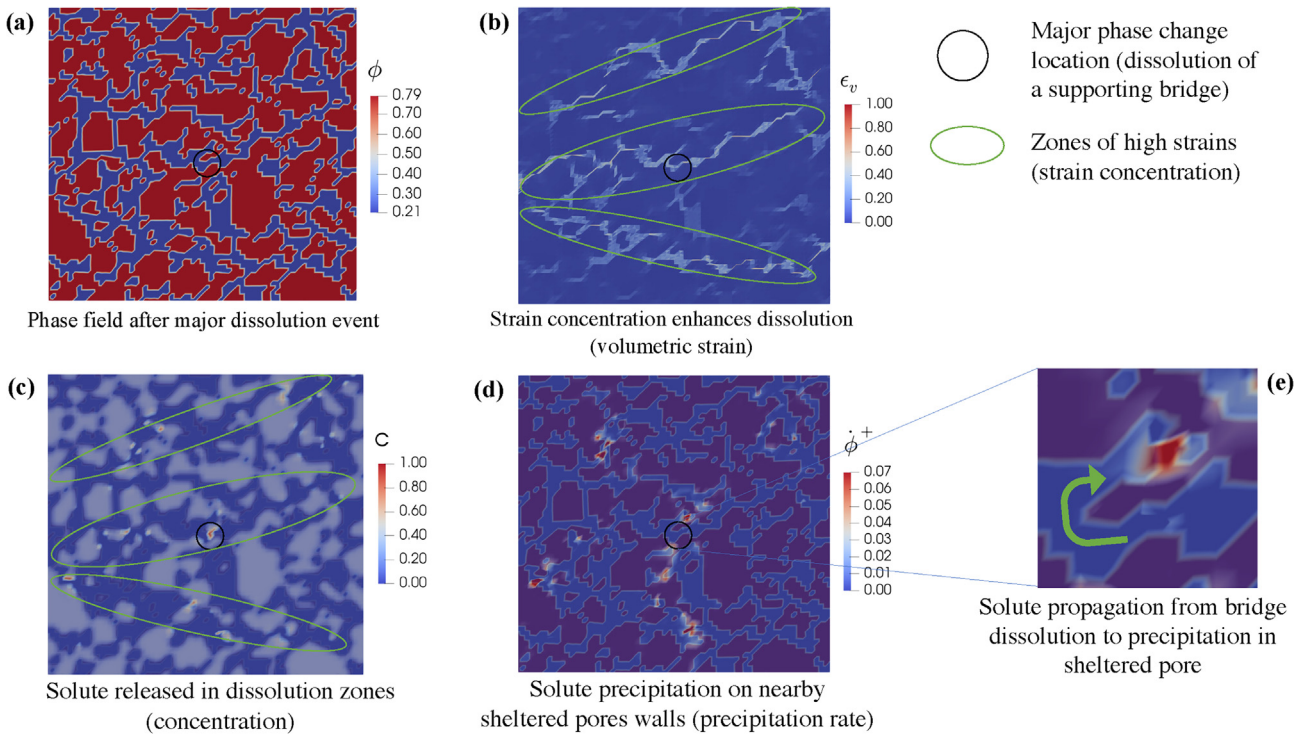

Fig. 10. Visualization of the microstructure's state of CT-scan #159 from Dong and Blunt (2009) at $t = 8.1$ at the end of a major phase change (dissolution of a supporting bridge in the center, indicated by the black circle). (a) Order parameter ϕ. (b) Volumetric strain ϵ_v. (c) Solute concentration c. (d) Positive part of order parameter rate $\dot{\phi}^+$ showing the precipitation zones. (e) Zoom-in on the bridge dissolution area: right after the bridge dissolution, the solute precipitates in a neighboring sheltered pore. The phase-field distribution (a) is superposed by transparency in (c) and (d). All in all, the particular microstructural geometry drives the strain concentration, which drives the dissolution/precipitation.

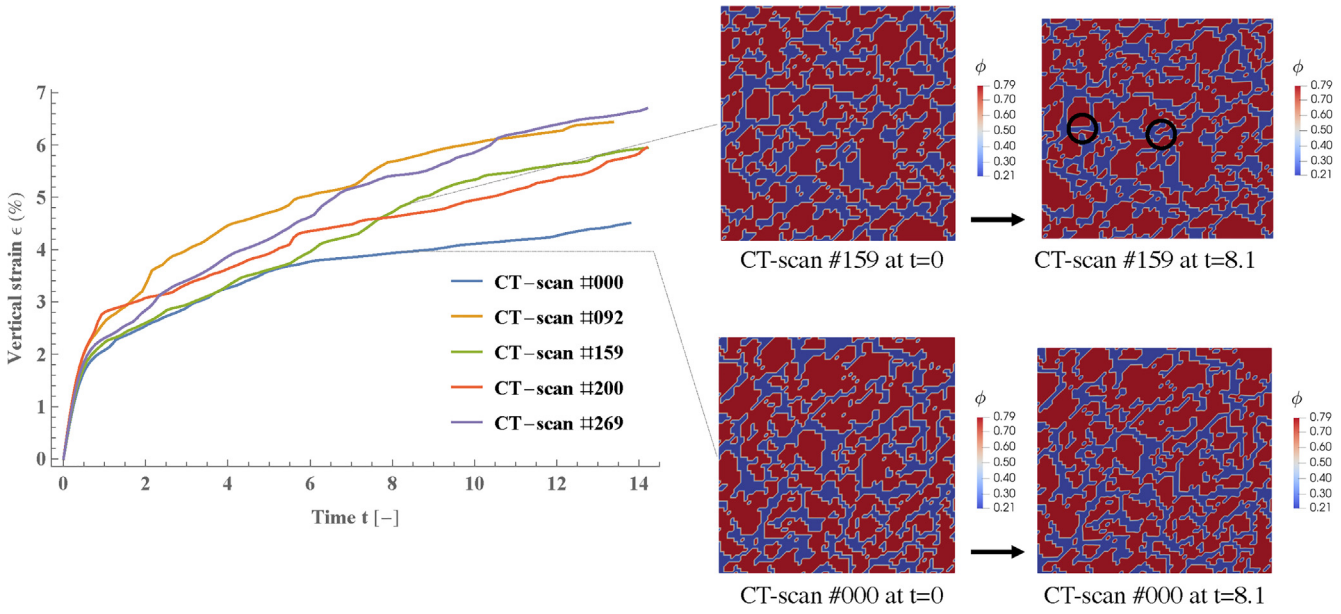

Fig. 11. Different creep responses of 5 different layers of the same sample (from Dong and Blunt, 2009) under oedometric vertical compression. Left panel: Vertical strain versus time. Right panel: visualization of the evolution of the microstructure (via ϕ) for CT-scans #159 and #000. Dissolution mainly affects the sharp edges (see left black circle) but also the supporting bridges (see right black circle) leading to a jump in the vertical strain (see green curve between $t = 7$ and $t = 9$). The CT-scan #000 shows negligible microstructural changes, in agreement with a vertical strain response with no jumps.

the Arrhenius law. In the case of temperature increase, μ would consistently decrease. In the case of the presence of catalytic constituents, such as clay for pressure solution, the activation energy Q of the reaction, and therefore μ, would decrease.

We propose similar conclusions for the dependence of pressure solution on temperature. Niemeijer et al. (2002) performed compaction creep experiments on quartz sand under different conditions, in particular with varying temperature, which experimental data set is reported in Fig. 13(b). A similar influence is observed for varying applied effective pressure. Note that in the particular case of the experimental results Fig. 13(b) an Andrade fitting is not as clear as the ones reported in Fig. 13(d).

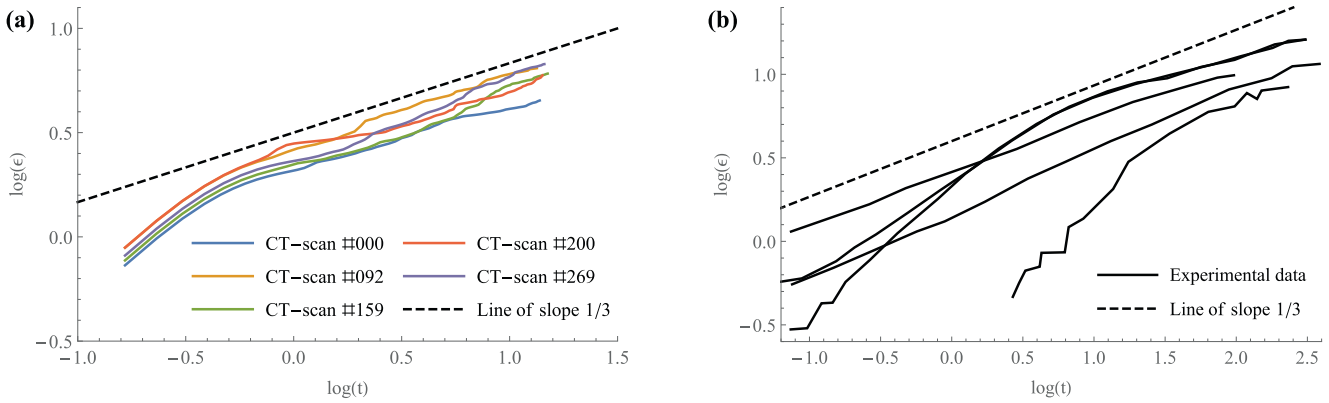

Fig. 12. Decimal logarithm of the vertical strain ϵ (%) versus decimal logarithm of time. (a) Numerical results from our model for 6 different CT-scan layers. (b) Experimental results from Dysthe et al. (2002) with halite for different surface treatments and brine volume. A line of slope 1/3 is associated to show the correspondence both numerically and experimentally with the Andrade creep law. The comparison is however only qualitative as the numerical results are dimensionless unlike the experimental ones. Hence we have normalized the displacement values of Dysthe et al. (2002) with an arbitrary reference length of 100 μm to obtain a strain and normalized the time values with an arbitrary value of 1 h. Similarly to Dysthe et al. (2002), we have removed the initial loading stage needed to establish the nominal contact for pressure solution, which we consider to last until the third time step for $t \approx 0.17$.

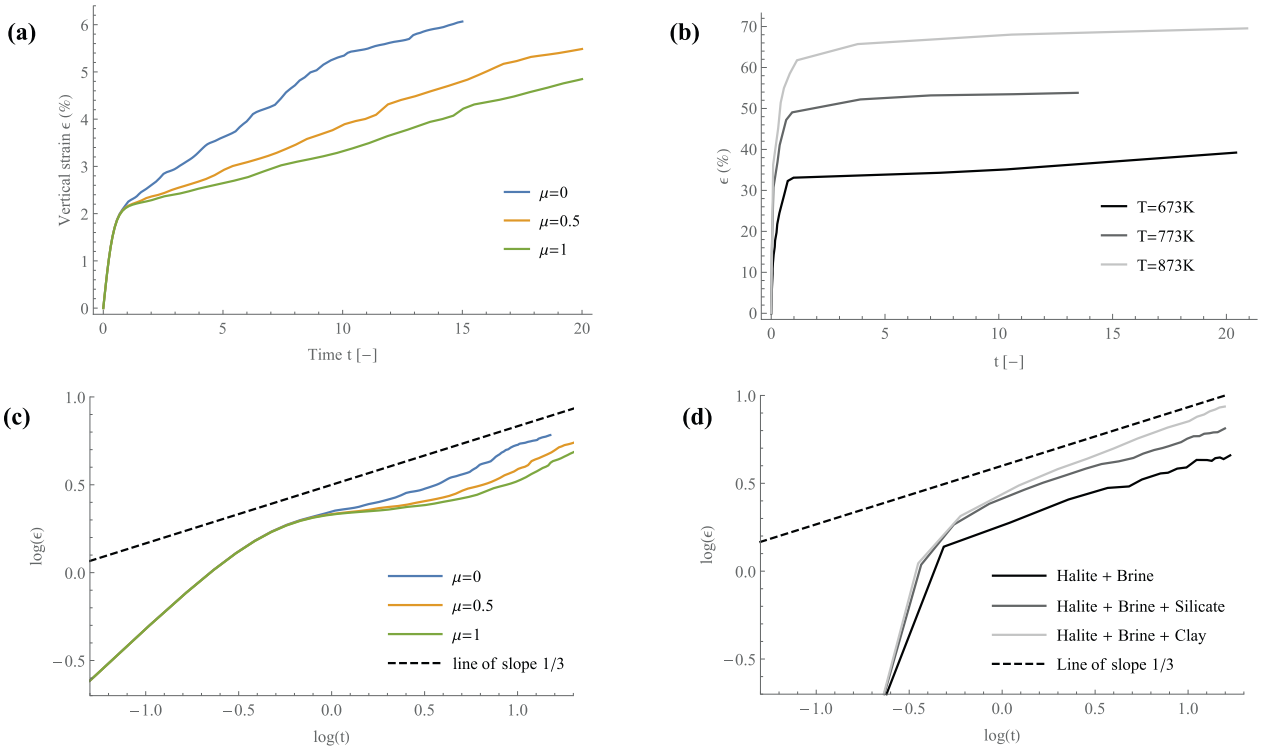

Fig. 13. Influence of the phase-field viscosity μ on the creep response under pressure solution (CT-scan #159). (a) Vertical strain versus time. (b) Experimental measurements from Niemeijer et al. (2002) on quartz sand with varying temperature. For comparison, we made the assumption that the strain evolution can be approximated by the porosity evolution. Clearly increasing temperature enhances pressure solution, characterized by a vertical translation of the response. Note that for comparison, we have normalized the time measurements from Niemeijer et al. (2002) by $t_0 = 7$ h. (c) Logarithmic strain versus logarithmic time. A decrease of μ, while preserving the Andrade creep response (line of slope 1/3), leads to an increase of the y-intercept of the Andrade creep part, i.e. a change of compaction rates. (d) Experimental measurements from Renard et al. (2001) on halite under pressure solution, comparing pores saturated with brine only, with brine and silicate and with brine and clay. Similarly, catalytic effects also increase the compaction rate while preserving an Andrade creep response. The time values of Renard et al. (2001) are normalized by the arbitrary value 10 h. Note that in Renard et al. (2001), the fitting power law's exponent was chosen as 0.4, yet an exponent of 1/3 remains satisfying.

5. Conclusion

We have introduced a framework to model geomaterials' microstructures by using a viscous phase-field model, with focus on a usually overlooked term, the phase-field viscosity. Our approach is consistently derived from contact thermodynamics, allowing all the state variables to be dissipative. This self-contained and systematic derivation from the generalized relaxation equation, equivalent to the dissipation inequality, allows for a straightforward coupling of the different mechanisms, such

as mechanics and chemistry in our case. In particular, the non-symmetric relaxation tensor, generalization of Onsager's symmetric phenomenological tensor, allows for an antisymmetric component, yielding a gyroscopic force, that proves useful in deriving a thermodynamically-consistent chemical coupling.

The main insight obtained from our theoretical and numerical study is that when explicitly tracking the microstructure of a material, as with phase-field modeling, and provided that its dynamics is allowed to be fully dissipative, the resulting microstructural viscosity renders the material's upscaled behavior rate-dependent. This could thus provide a microphysical support to viscoplasticity, which essentially upscales the viscosity of the microstructure. Rate-dependency is characteristic of materials with microstructure, all the more when the latter is highly irregular as that of geomaterials.

To illustrate the influence of the microstructure, we have studied pressure solution creep. It is largely acknowledged that pressure solution, because of the constant loading and tight chemo-mechanical coupling, is a transient process owing to the ceaseless grain boundary dynamics. Therefore, the usual steady states models are very limiting. We have observed numerically, as intuited from the phase-field theory, that the Laplacian rate term controls the change of curvature of the interface, or more exactly its change of orientation. This seems to mitigate potential loss of smoothness of the interface upon high deformation. In the context of dissolution, while the rate of the order parameter, measuring the interface's normal variations, can be seen as the volumetric component of the dissolution of a grain, including the Laplacian rate can be seen as completing the description of the dissolution with its deviatoric component. From a macroscopic point of view, the corresponding phase-field viscosity can encapsulate catalytic effects such as temperature and the presence of clay. More generally, controlling such kinetic parameters could help accessing field conditions from the laboratory conditions. Specifically, after calibrating the microstructural viscosity in the laboratory at a certain time scale and temperature, one could deduce the corresponding behavior at the field's time scale and temperature, provided that the microstructure is representative. This could be of interest for materials used in engineering, such as cement (Bazant et al., 2004), barrier clays (Veveakis and Poulet, 2020) and energy-related geomaterials (Veveakis and Regenauer-lieb, 2015; Alevizos et al., 2017), for which the microstructural chemical reactions (like pressure solution) are taking place at a much slower rate than those of halite and quartz.

In further works, we shall focus on quantitatively corroborating our model with experimental results. Firstly, this should allow us to more realistically calibrate the model's parameters. Secondly, we should be able to address the effect of the grainsize distribution and numerically display the preliminary insights found in the literature. Thirdly, we may illustrate the time-dependency induced by the phase-field viscosity by its ability to capture catalytic effects such as heating and the presence of clay. That way, we may be able to check the validity of the usual constitutive creep laws, in particular the grainsize exponent, as well as potentially generalize them to include rate-dependency and catalytic effects. Further obvious improvements include performing 3D simulations, as well as modeling the fluid flow in the pores, which could be crucial in modeling pore pressure build-up that could trigger frictional instability.

CRediT authorship contribution statement

A. Guével: Conceptualization, Methodology, Software, Formal analysis, Investigation, Data curation, Writing - original draft, Visualization. **H. Rattez:** Conceptualization, Software, Validation, Writing - review & editing, Visualization. **E. Veveakis:** Conceptualization, Validation, Writing - review & editing, Supervision.

Declaration of Competing Interest

The authors declare that they have no known competing financial interests or personal relationships that could have appeared to influence the work reported in this paper.

Acknowledgement

The authors Alexandre Guével and Manolis Veveakis acknowledge the support of US DOE grant DE-NE0008746, and the Australian ARC grants DP170104550, DP170104557. This work was also supported by the Southern California Earthquake Center (SCEC), award number 118062196. SCEC is funded by NSF Cooperative Agreement EAR-1033462 and USGS Cooperative Agreement G12AC20038. We are indebted to Prof. Eliot Fried for sharing with us his extensive expertise on the theoretical foundations of thermodynamics and phase-field modeling. We thank Martin Lesueur and Thomas Poulet for helping in the numerical simulations. We also thank Sotiris Alevizos for all the insightful discussions in the preliminary stage. Finally, we acknowledge the significant contributions of the Editor, Prof. Chad Landis, and Prof. Chris Spiers during the review process, which improved the manuscript substantially.

Appendix A. Dissipative and non-dissipative parts of the relaxation tensor

Upon decomposing $\boldsymbol{\tau}$ into its symmetric part $\boldsymbol{\tau}^s$ and asymmetric part $\boldsymbol{\tau}^a$, the dissipation $D \equiv \boldsymbol{X}\cdot\dot{\boldsymbol{x}} \geqslant 0$ can be written as:

$$D = \boldsymbol{\tau}^s\dot{\boldsymbol{x}}\cdot\dot{\boldsymbol{x}} + \boldsymbol{\tau}^a\dot{\boldsymbol{x}}\cdot\dot{\boldsymbol{x}}. \tag{A.1}$$

The second scalar product can be written $\boldsymbol{\tau}^a\dot{\boldsymbol{x}}\cdot\dot{\boldsymbol{x}} = \dot{\boldsymbol{x}}\cdot\boldsymbol{\tau}^{aT}\dot{\boldsymbol{x}} = -\dot{\boldsymbol{x}}\cdot\boldsymbol{\tau}^a\dot{\boldsymbol{x}} = -\boldsymbol{\tau}^a\dot{\boldsymbol{x}}\cdot\dot{\boldsymbol{x}}$ so that:

$$\boldsymbol{\tau}^a\dot{\boldsymbol{x}}\cdot\dot{\boldsymbol{x}} = 0. \tag{A.2}$$

The thermodynamic forces vector can thus be decomposed into a dissipative part characterized by the symmetric part of $\boldsymbol{\tau}$ and a non-dissipative part characterized by the non-symmetric part of $\boldsymbol{\tau}$:

$$\boxed{\boldsymbol{X} = \boldsymbol{\tau}^s\dot{\boldsymbol{x}} + \boldsymbol{\tau}^a\dot{\boldsymbol{x}} = \boldsymbol{X}^d + \boldsymbol{X}^{nd}}. \tag{A.3}$$

Upon identifying our unique decomposition of the thermodynamic forces vector $\boldsymbol{X}$ with Edelen's unique decomposition (Edelen, 1977), we deduce

$$\begin{cases} \boldsymbol{X}^d = \boldsymbol{\tau}^s\dot{\boldsymbol{x}} = \frac{\partial\Phi}{\partial\dot{\boldsymbol{x}}} \\ \boldsymbol{X}^{nd} = \boldsymbol{\tau}^a\dot{\boldsymbol{x}} = \boldsymbol{U}. \end{cases} \tag{A.4}$$

Thus, one can equivalently define the dissipative part $\boldsymbol{X}^d$ via $\boldsymbol{\tau}^s$ or the dissipation potential Φ, and the non-dissipative part $\boldsymbol{X}^{nd}$ via $\boldsymbol{\tau}^a$ or the gyroscopic force $\boldsymbol{U}$.

Appendix B. Numerical solution of the viscous Allen–Cahn equation in 1D

To appreciate the effect of the phase-field viscosity μ, we solve numerically (on *Mathematica*) the 1D problem in the simplest setting with the double-well potential without energy input ($\chi = 0$):

$$-\mu\frac{\partial^3\phi}{\partial x^2\partial t} + \frac{\partial\phi}{\partial t} = \alpha\frac{\partial^2\phi}{\partial x^2} - 2\phi(1 - 3\phi + 2\phi^2) \tag{B.1}$$

where we recall that the derivative of the double-well function reads $g'(\phi) = 2\phi(1-3\phi+2\phi^2)$. We solve this equation associated with the initial condition $\phi(x, t=0) = \phi_0 \in \{0.49, 0.51\}$ and the two boundary conditions $\phi(x=0,t) = \phi(x=1,t) = \phi_0$. We visualize in Fig. (14) the evolution of the point $x = 1/2$. As expected, an initial state $\phi = 0.51$ converges to the closest stable steady state $\phi = 1$ whereas an initial state $\phi = 0.49$ converges to the closest steady state $\phi = 0$. Most interestingly, we can see that as μ increases, the steady state is delayed.

Appendix C. Curvature as a function of the phase field

We make the postulate in the present numerical study that the Laplacian of the order parameter $\triangle\phi$ describes, at least partly, a measure of the local curvature. Although so-called sharp-interface quantities such as curvature should be formally related to phase-field quantities via a matched asymptotic analysis, we propose as a partial justification the following consideration.

In the present phase-field context, the level sets are also called uniformity surfaces (Fried and Gurtin, 1996) and are defined as follows:

$$\mathscr{S}_a = \left\{(x,y,x) \in \mathbb{R}^3 | \phi(x,y,z) = a\right\},\ 0.21 \leqslant a \leqslant 0.79 \tag{C.1}$$

where (x,y,z) is the Cartesian position vector and a a constant in $[0.21, 0.79]$. Note that we implicitly consider the dependence on time here. One can use the gradient of the order parameter to define the non-unit normal to the uniformity surfaces $\boldsymbol{n} \equiv \nabla\phi$ and the unit normal $\hat{\boldsymbol{n}} \equiv \frac{\nabla\phi}{||\nabla\phi||}$. Then, one can show that the local mean curvature κ reads:

$$\kappa = -\nabla \cdot \hat{\boldsymbol{n}}. \tag{C.2}$$

The minus is chosen here by convention. More precisely, in 2D, $-\nabla \cdot \hat{\boldsymbol{n}}$ is equal to the differentiation of the angle between the horizontal and the tangent to the curve, with respect to the arc length. In 3D, $-\nabla \cdot \hat{\boldsymbol{n}}$ is the sum of the two principal curvatures of the surface. Thereupon one can show that:

$$\kappa = -\frac{1}{||\nabla\phi||}(\triangle\phi - (\nabla\nabla\phi)\hat{\boldsymbol{n}} \cdot \hat{\boldsymbol{n}}). \tag{C.3}$$

The connection between κ and $\triangle\phi$ boils down to this relation in the general case. However, in 2D, one can show that it reduces to:

$$\kappa = -\frac{\phi_{xx}\phi_y^2 - 2\phi_x\phi_y\phi_{xy} + \phi_{yy}\phi_x^2}{\left(\phi_x^2 + \phi_y^2\right)^{3/2}} \tag{C.4}$$

where we use the usual notation for derivatives. Since this equation is left unchanged upon interchanging x and y, we can define without loss of generality:

$$\phi(x,y) = y - f(x) \tag{C.5}$$

with f a smooth function of x. We then obtain:

$$\kappa = -\frac{f''(x)}{\left(1 + f'(x)^2\right)^{3/2}}. \tag{C.6}$$

Therefore, for sufficiently small slopes of the interface function f, this yields the approximation in 2D:

$$\kappa \approx \triangle\phi. \tag{C.7}$$

Finally, one could argue that the definition of the curvature κ could be loosened to describe the curvature with the non-unit normal vector $\boldsymbol{n}$ instead of the unit normal vector $\hat{\boldsymbol{n}}$, insofar as they both describe the orientation of the interface. In that case, $\triangle\phi = -\nabla \cdot \boldsymbol{n}$ indeed characterizes the notion of curvature of the interface.

Appendix D. Summary of the numerical parameters' values

The parameters of the model and their assigned numerical values in the different simulations are summarized in the table below. We remind that we use the following consistent units system: *ks* for times, *mm* for lengths, *GPa* (i.e. J/mm^3) for stresses (i.e. specific energies) and *kg* for masses. When no unit is indicated, the quantity is dimensionless. We use an asterisk to differentiate a dimensionless quantity from its dimensioned counterpart, although asterisk notation is dropped in the text body.

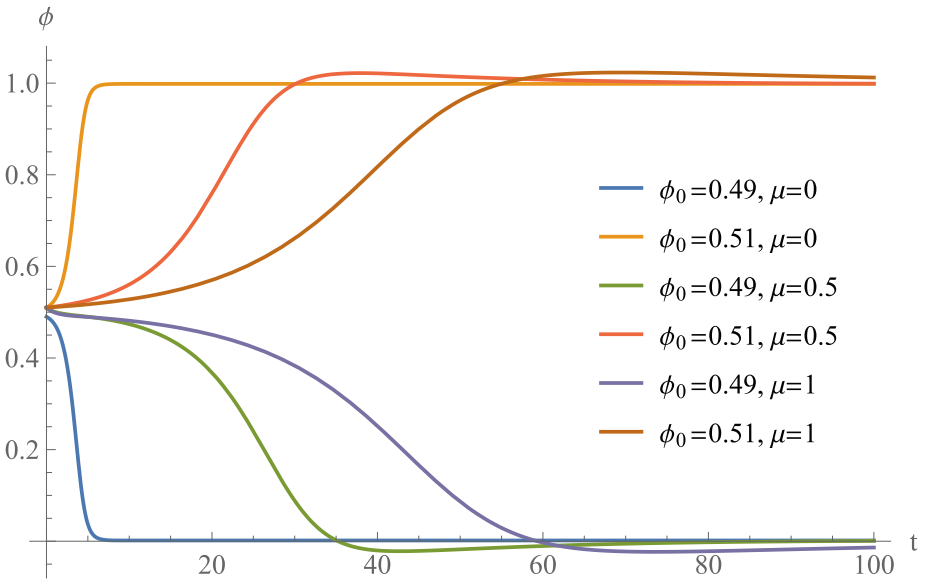

Fig. 14. Numerical solution of Eq. (B.1) in 1D for varying μ.

Parameters vs Simulations		3.2.1	3.2.2	3.2.3	4.1	4.2
$l_0[mm]$	Problem's length scale	0.3	0.3	0.3	3	3
$t_0 \equiv \frac{\tau_1}{G}[ks]$	Problem's time scale	1	1	1	1	1
G [GPa]	Problem's stress scale	1	1	1	1	1
$\mu \equiv \frac{\tau_2 G}{\tau_1 l_0^2}$	Phase-field viscosity	0	Varying	0	Varying	Varying
$\alpha \equiv \frac{\kappa}{G l_0^2} \sim \frac{l_1^2}{l_0^2} \sim \frac{\gamma^2}{G^2 l_0^2}$	Interface coefficient	0.1	0.1	0.1	0.01	0.01
$\lambda_A^* \equiv \frac{\lambda_A}{G}$	1^{st} Lamé parameter for phase A	1	1	1	1	1
$\mu_A^* \equiv \frac{\mu_A}{G}$	2^{nd} Lamé parameter for phase A	0	0	0	0	0
$\lambda_B^* \equiv \frac{\lambda_B}{G}$	1^{st} Lamé parameter for phase B	30	30	30	30	30
$\mu_B^* \equiv \frac{\mu_B}{G}$	2^{nd} Lamé parameter for phase B	30	30	30	30	30
$\beta^* \equiv \frac{\beta}{G}$	Chemical coupling coefficient	0	0	0.05	0	5
$\tau_c \equiv \frac{\tau_3}{G t_0}$	Chemical relaxation time	0	0	1	0	1
$D^* \equiv \frac{D}{G l_0^2}$	Chemical diffusivity	0	0	10	0	0.1
$\tau_m \equiv \frac{\tau_5}{G t_0}$	Mechanical relaxation time	0	0	0	0	0
Loading	Displacement-controlled for 3.2.1, 3.2.2, 4.1 and stress-controlled for 3.2.3, 4.2	$1 \times t$	$1 \times t$	$0.2\tanh(2t)$	$1 \times t$	$0.5\tanh(2.3t)$

References

Aagesen, L.K., Schwen, D., Ahmed, K., Tonks, M.R., 2017. Quantifying elastic energy effects on interfacial energy in the Kim-Kim-Suzuki phase-field model with different interpolation schemes. Comput. Mater. Sci. 140, 10–21. https://doi.org/10.1016/j.commatsci.2017.08.005.

Alevizos, S., Poulet, T., Sari, M., Lesueur, M., Regenauer-Lieb, K., Veveakis, M., 2017. A framework for fracture network formation in overpressurised impermeable shale: deformability versus diagenesis. Rock Mech. Rock Eng. 50 (3), 689–703. https://doi.org/10.1007/s00603-016-0996-y.

Allen, S.M., Cahn, J.W., 1979. A microscopic theory for antiphase boundary motion and its application to antiphase domain coarsening. Acta Metall. 27 (6), 1085–1095. https://doi.org/10.1016/0001-6160(79)90196-2.

Ammar, K., Appolaire, B., Cailletaud, G., Forest, S., 2009. Combining phase field approach and homogenization methods for modelling phase transformation in elastoplastic media. Revue européenne de mécanique numérique 18 (5–6), 485–523. https://doi.org/10.3166/ejcm.18.485-523. URL: http://ejcm.revuesonline.com/article.jsp?articleId=14048.

Andrade, E.N.D.C., 1910. On the viscous flow in metals and allied phenomena. Proc. R. Soc. London A 84, 1–12. https://doi.org/10.1098/rspa.1910.0050.

Arnold, V.I., 1978. Mathematical Methods of Classical Mechanics. Springer, New York, NY. https://doi.org/10.1007/978-1-4757-2063-1.

Arnold, V.I., 1990. Contact Geometry: the Geometrical Method of Gibbs's Thermodynamics, in. Proc. Gibbs Symposium, 163–179.

Barenblatt, G.I., Zheltov, I.P., Kochina, I.N., 1960. Basic concepts in the theory of seepage of homogeneous liquids in fissured rocks [strata]. J. Appl. Math. Mech. 24 (5), 1286–1303. https://doi.org/10.1016/0021-8928(60)90107-6.

Bazant, Z.P., Cusatis, G., Cedolin, L., 2004. Temperature effect on concrete creep modeled by microprestress-solidification theory. J. Eng. Mech. 130, 691–699. https://doi.org/10.1061/(ASCE)0733-9399(2004)130. URL: http://link.aip.org/link/?JENMDT/130/1195/1.

Borden, M.J., Verhoosel, C.V., Scott, M.A., Hughes, T.J., Landis, C.M., 2012. A phase-field description of dynamic brittle fracture. Comput. Methods Appl. Mech. Eng. 217–220, 77–95. https://doi.org/10.1016/j.cma.2012.01.008.

Cahn, J.W., 1961. On spinodal decomposition. Acta mechanica 9, 795–801. https://doi.org/10.1016/0001-6160(61)90182-1.

Cahn, J.W., Hilliard, J.E., 1958. Free energy of a nonuniform system. I. Interfacial free energy. J. Chem. Phys. 28 (2), 258–267. https://doi.org/10.1063/1.1744102. arXiv:9809069v1.

Carlsson, J., Isaksson, P., 2020. A statistical geometry approach to length scales in phase field modelling of fracture and strength of porous microstructures. Int. J. Solids Struct. 200–201, 83–93. https://doi.org/10.1016/j.ijsolstr.2020.05.003. URL:https://doi.org/10.1016/j.ijsolstr.2020.05.003.

Chen, L.-Q., Khachaturyan, A.G., 1991. Computer simulation of structural transformations during precipitation of an ordered intermetallic phase. Acta Metall. Mater. 39 (11), 2533–2551. https://doi.org/10.1016/0956-7151(91)90069-D.

Coleman, B.D., Noll, W., 1963. The thermodynamics of elastic materials with heat conduction and viscosity. Arch. Ration. Mech. Anal. 13 (1), 167–178. https://doi.org/10.1007/bf01262690.

Collins, I.F., Houlsby, G.T., 1997. Application of thermomechanical principles to the modelling of geotechnical materials. Proc. R. Soc. A: Math., Phys. Eng. Sci. 453 (1964), 1975–2001. https://doi.org/10.1098/rspa.1997.0107.

Coussy, O., 2004. Poromechanics. Wiley.

Croizé, D., Renard, F., Gratier, J.P., 2013. Compaction and Porosity Reduction in Carbonates: A Review of Observations, Theory, and Experiments. In: Advances in Geophysics, vol. 54, Elsevier Inc., pp. 181–238.https://doi.org/10.1016/B978-0-12-380940-7.00003-2..

Cueto-Felgueroso, L., Juanes, R., 2009. A phase field model of unsaturated flow. Water Resour. Res. 45 (10), 1–23. https://doi.org/10.1029/2009WR007945. arXiv:2014WR016527.

de Boer, R.B., Nagtegaal, P.J., Duyvis, E.M., 1977. Pressure solution experiments on quartz sand. Geochim. Cosmochim. Acta 41 (2). https://doi.org/10.1016/0016-7037(77)90233-2.

Desrues, J., Chambon, R., Mokni, M., Mazerolle, F., 1996. Void ratio evolution inside shear bands in triaxial sand specimens studied by computed tomography. Geotechnique 46 (3), 529–546. https://doi.org/10.1680/geot.1996.46.3.529.

Detournay, E., Cheng, A.H., 1993. Fundamentals of poroelasticity, Comprehensive rock engineering. vol. 2 I I, pp. 113–171.https://doi.org/10.1017/cbo9781139051132.003..

Dijk, N.P., Espadas-Escalante, J.J., Isaksson, P., 2020. Strain energy density decompositions in phase-field fracture theories for orthotropy and anisotropy. Int. J. Solids Struct. 196–197, 140–153. https://doi.org/10.1016/j.ijsolstr.2020.04.022.

Dong, H., Blunt, M.J., 2009. Pore-network extraction from micro-computerized-tomography images. Phys. Rev. E – Stat., Nonlinear, Soft Matter Phys. 80 (3), 1–11. https://doi.org/10.1103/PhysRevE.80.036307.

Dysthe, D.K., Podladchikov, Y., Renard, F., Feder, J., Jamtveit, B., 2002. Universal scaling in transient creep. Phys. Rev. Lett. 89 (24), 1–4. https://doi.org/10.1103/PhysRevLett.89.246102.

Edelen, D.G.B., 1977. General solution of the dissipation inequality. J. Non-Equilib. Thermodyn. 2 (4), 205–210. https://doi.org/10.1515/jnet.1977.2.4.205.

Edelen, D., 1993. The College Station Lectures on Thermodynamics. Texas A & M University, College Station Texas.

Fix, G.J., 1983. Free boundary problems: theory and applications, Vol. II, Pitman Advanced Publishing Program (Research Notes in Mathematics 79), 1983. arXiv: arXiv:1011.1669v3,https://doi.org/10.1017/CBO9781107415324.004..

Fried, E., 2006. On the relationship between supplemental balances in two theories for pure interface motion. SIAM J. Appl. Math. 66 (4), 1130–1149.

Fried, E., Gurtin, M.E., 1993. Continuum theory of thermally induced phase transitions based on an order parameter. Physica D 68 (3–4), 326–343. https://doi.org/10.1016/0167-2789(93)90128-N.

Fried, E., Gurtin, M.E., 1994. Dynamic solid-solid transitions with phase characterized by an order parameter. Physica D 72 (4), 287–308. https://doi.org/10.1016/0167-2789(94)90234-8.

Fried, E., Gurtin, M.E., 1996. A phase-field theory for solidification based on a general anisotropic sharp-interface theory with interfacial energy and entropy. Physica D 91 (1), 143–181. https://doi.org/10.1016/0167-2789(95)00121-2.

Gaston, D., Hansen, G., Newman, C., 2009. MOOSE: A parallel computational framework for coupled systems of nonlinear equations, American Nuclear

Society – International Conference on Mathematics, Computational Methods and Reactor Physics 2009, M and C 2009 1, pp. 224–233..
Geiges, H., 2008. An Introduction to Contact Topology. Cambridge University Press.
Ghoussoub, J., Leroy, Y.M., 2001. Solid-fluid phase transformation within grain boundaries during compaction by pressure solution. J. Mech. Phys. Solids 49 (10), 2385–2430. https://doi.org/10.1016/S0022-5096(01)00012-6.
Ginzburg, V., Landau, L., 1950. On the theory of superconductivity. Zh. Eksp. Teor. Fiz. 20, 1064–1082.
Goddard, J.D., 2014. Edelen's dissipation potentials and the visco-plasticity of particulate media. Acta Mech. 225 (8), 2239–2259. https://doi.org/10.1007/s00707-014-1123-3.
Gratier, J.P., Dysthe, D.K., Renard, F., 2013. The Role of Pressure Solution Creep in the Ductility of the Earth's Upper Crust, vol. 54, Elsevier Inc.https://doi.org/10.1016/B978-0-12-380940-7.00002-0..
Griggs, D., 1940. Experimental flow of rocks under conditions favoring recrystallization. Bull. Geol. Soc. Am. 51 (7), 1001–1022. https://doi.org/10.1130/GSAB-51-1001.
Gundersen, E., Dysthe, D.K., Renard, F., Bjorlykke, K., Jamtveit, B., 2002. Numerical modelling of pressure solution in sandstone, rate-limiting processes and the effect of clays. Geological Society, London, Special Publications 200 (1), 41–60. https://doi.org/10.1144/GSL.SP.2001.200.01.03. URL: http://sp.lyellcollection.org/cgi/doi/10.1144/GSL.SP.2001.200.01.03.
Gurtin, M.E., 1996. Generalized Ginzburg-Landau and Cahn-Hilliard equations based on a microforce balance. Physica D 92 (3–4), 178–192. https://doi.org/10.1155/S1110757X03204083.
Gurtin, M.E., 2000. Configurational Forces as Basic Concepts of Continuum Physics. Springer, New York, NY.
Haslach, H.W.J., 1997. Geometric structure of the non-equilibrium thermodynamics of homogeneous systems. Rep. Math. Phys. 39. https://doi.org/10.1016/S0034-4877(97)87997-9. URL: http://www.sciencedirect.com/science/article/pii/S0034487797879979.
Heald, M.T., 1956. Cementation of Simpson and St. Peter Sandstones in Parts of Oklahoma, Arkansas, and Missouri. J. Geol. 64 (1), 16–30.
Heider, Y., Sun, W.C., 2020. A phase field framework for capillary-induced fracture in unsaturated porous media: drying-induced vs. hydraulic cracking. Comput. Methods Appl. Mech. Eng. 359,. https://doi.org/10.1016/j.cma.2019.112647 112647.
Hermann, R., 1973. Geometry, Physics, and Systems. Marcel Dekker.
Kassner, K., Misbah, C., Müller, J., Kappey, J., Kohlert, P., 2001. Phase-field modeling of stress-induced instabilities. Phys. Rev. E – Statist. Phys., Plasmas, Fluids, Related Interdisciplinary Topics 63 (3), 1–27. https://doi.org/10.1103/PhysRevE.63.036117.
Kawamoto, R., Andò, E., Viggiani, G., Andrade, J.E., 2018. All you need is shape: predicting shear banding in sand with LS-DEM. J. Mech. Phys. Solids 111 (November), 375–392. https://doi.org/10.1016/j.jmps.2017.10.003.
Kim, S.G., Kim, W.T., Suzuki, T., 1999. Phase-field model for binary alloys. Phys. Rev. E – Stat. Phys., Plasmas, Fluids, Related Interdisciplinary Topics 60 (6), 7186–7197. https://doi.org/10.1103/PhysRevE.60.7186.
Landau, L.D., 1937. On the theory of phase transitions. Zh. Eks. Teor. Fiz. 7 (1937), 19–32. https://doi.org/10.1038/138840a0.
Landau, L., Khalatnikov, I.M., 1965. On the anomalous absorption of sound near a second order phase transition point (English translation in Collected Papers of Landau, edited by D. Ter Haar, 1965). Dokl. Akad. Nauk. SSSR 96, 469.
Langer, J.S., 1986. Models of pattern formation in first-order phase transitions. World Scientific.
Lehner, F.K., 1995. A model for intergranular pressure solution in open systems. Tectonophysics 245 (3–4), 153–170. https://doi.org/10.1016/0040-1951(94)00232-X.
Lehner, F.K., Bataille, J., 1984. Nonequilibrium thermodynamics of pressure solution. Pure Appl. Geophys. PAGEOPH 122 (1), 53–85. https://doi.org/10.1007/BF00879649.
Lesueur, M., Poulet, T., Veveakis, M., 2020. Three-scale multiphysics finite element framework (FE 3) modelling fault reactivation. Comput. Methods Appl. Mech. Eng. 365,. https://doi.org/10.1016/j.cma.2020.112988 112988.
Lowry, W.D., 1956. Factors in loss of porosity by quartzose sandstones in Virginia. Bull. Amer. Assoc. Petrol. Geol. 40, 489–500.
Mrugala, R., 1978. Geometrical formulation of equilibrium phenomenological thermodynamics. Rep. Math. Phys. 14 (3), 419–427. https://doi.org/10.1016/0034-4877(78)90010-1.
Niemeijer, A.R., Spiers, C.J., Bos, B., 2002. Compaction creep of quartz sand at 400–600 C: experimental evidence for dissolution-controlled pressure solution. Earth Planet. Sci. Lett. 195 (3–4), 261–275. https://doi.org/10.1016/S0012-821X(01)00593-3.
Niemeijer, A., Elsworth, D., Marone, C., 2009. Significant effect of grain size distribution on compaction rates in granular aggregates. Earth Planet. Sci. Lett. 284 (3–4), 386–391. https://doi.org/10.1016/j.epsl.2009.04.041.
Ostoja-Starzewski, M., 2009. A derivation of the Maxwell-Cattaneo equation from the free energy and dissipation potentials. Int. J. Eng. Sci. 47 (7–8), 807–810. https://doi.org/10.1016/j.ijengsci.2009.03.002.
Ostoja-Starzewski, M., Malyarenko, A., 2014. Continuum mechanics beyond the second law of thermodynamics. Proc. R. Soc. A: Math. Phys. Eng. Sci. 470 (2171). https://doi.org/10.1098/rspa.2014.0531.
O'Sullivan, C., 2011. Particulate Discrete Element Modelling: a Geomechanics Perspective. Spon Press.
Poulet, T., Veveakis, M., Herwegh, M., Buckingham, T., Regenauer-Lieb, K., 2014. Modeling episodic fluid-release events in the ductile carbonates of the Glarus thrust. Geophys. Res. Lett. 41 (20), 7121–7128. https://doi.org/10.1002/2014GL061715.
Poulet, T., Paesold, M., Veveakis, M., 2017. Multi-physics modelling of fault mechanics using REDBACK: a parallel open-source simulator for tightly coupled problems. Rock Mech. Rock Eng. 50 (3), 733–749. https://doi.org/10.1007/s00603-016-0927-y.
Raj, R., 1982. Creep in polycrystalline aggregates by matter transport through a liquid phase. J. Geophys. Res. 87, 4731–4739.
Raj, R., Chyung, C.K., 1981. Solution-precipitation creep in glass ceramics. Acta Metall. 29, 159–166.
Rattez, H., Veveakis, M., 2020. Weak phases production and heat generation control fault friction during seismic slip. Nat. Commun. 11 (1), 1–8. https://doi.org/10.1038/s41467-019-14252-5.
Rattez, H., Stefanou, I., Sulem, J., 2018. The importance of Thermo-Hydro-Mechanical couplings and microstructure to strain localization in 3D continua with application to seismic faults. Part I: Theory and linear stability analysis. J. Mech. Phys. Solids 115 (March), 54–76. https://doi.org/10.1016/j.jmps.2018.03.004.
Rattez, H., Stefanou, I., Sulem, J., Veveakis, M., Poulet, T., 2018. The importance of Thermo-Hydro-Mechanical couplings and microstructure to strain localization in 3D continua with application to seismic faults. Part II: Numerical implementation and post-bifurcation analysis. J. Mech. Phys. Solids 115 (March), 1–29. https://doi.org/10.1016/j.jmps.2018.03.003.
Renard, F., Ortoleva, P., Gratier, J.P., 1997. Pressure solution in sandstones: influence of clays and dependence on temperature and stress. Tectonophysics 280 (3–4), 257–266. https://doi.org/10.1016/S0040-1951(97)00039-5.
Renard, F., Gratier, J.P., Jamtveit, B., 2000. Kinetics of crack-sealing, intergranular pressure solution, and compaction around active faults. J. Struct. Geol. 22 (10), 1395–1407. https://doi.org/10.1016/S0191-8141(00)00064-X.
Renard, F., Dysthe, D., Feder, J., Bjørlykke, K., Jamtveit, B., 2001. Enhanced pressure solution creep rates induced by clay particles: experimental evidence in salt aggregates. Geophys. Res. Lett. 28 (7), 1295–1298. https://doi.org/10.1029/2000gl012394.
Renton, J.J., Heald, M.T., Cecil, C.B., 1969. Experimental investigation of pressure solution of quartz. J. Sediment. Res. 39 (3), 1107–1117. https://doi.org/10.1306/74D71DA2-2B21-11D7-8648000102C1865D.
Rowlinson, J.S., 1979. Translation of J.D. van der Waals' The thermodynamik theory of capillarity under the hypothesis of a continuous variation of density. J. Stat. Phys. 20 (2), 197–200. https://doi.org/10.1007/BF01011513.
Schwarz, S., Stöckhert, B., 2002. Pressure solution in siliciclastic HP-LT metamorphic rocks — constraints on the state of stress in deep levels of accretionary complexes. Tectonophysics 255 (3–4), 203–209. https://doi.org/10.1016/0040-1951(95)00137-9.
Sciarra, G., 2016. Phase field modeling of partially saturated deformable porous media. J. Mech. Phys. Solids 94, 230–256. https://doi.org/10.1016/j.jmps.2016.04.018. arXiv:arXiv:1603.05564v1.
Shin, K., 2017. Possible effect of pressure solution on the movement of a canister in the buffer of geological disposal system. Int. J. Geosci. 08 (02), 167–180. https://doi.org/10.4236/ijg.2017.82006.
Sleep, N.H., Blanpied, M.L., 1992. Creep, compaction and the weak rheology of major faults. Nature 359 (6397), 687–692. https://doi.org/10.1038/359687a0.
Sorby, H.C., 1863. On the direct correlation of mechanical and chemical forces. In: Proceeding of the Royal Society of London, vol. 12, pp. 538–550.https://doi.org/10.1016/0016-0032(64)90404-1..
Talabi, O., AlSayari, S., Iglauer, S., Blunt, M.J., 2009. Pore-scale simulation of NMR response. J. Petrol. Sci. Eng. 67 (3–4), 168–178. https://doi.org/10.1016/j.petrol.2009.05.013.
Ting, T., 1969. Parabolic and pseudo-parabolic partial differential equations. J. Math. Soc. Japan 21 (3), 440–453. https://doi.org/10.2969/jmsj/02130440.
Tonks, M.R., Gaston, D., Millett, P.C., Andrs, D., Talbot, P., 2012. An object-oriented finite element framework for multiphysics phase field simulations. Comput. Mater. Sci. 51 (1), 20–29. https://doi.org/10.1016/j.commatsci.2011.07.028.
Toussaint, R., Aharonov, E., Koehn, D., Gratier, J.P., Ebner, M., Baud, P., Rolland, A., Renard, F., 2018. Stylolites: A review. J. Struct. Geol. 114 (July), 163–195. https://doi.org/10.1016/j.jsg.2018.05.003.
Truesdell, C., Toupin, R., 1960. The Classical Field Theories. Springer, Berlin Heidelberg, Berlin, Heidelberg, pp. 226–858. URL: https://doi.org/10.1007/978-3-642-45943-6_2.
Urai, J.L., Spiers, C.J., Zwart, H.J., Lister, G.S., 1986. Weakening of rock salt by water during long-term creep. Nature 324 (6097), 554–557. https://doi.org/10.1038/324554a0.
van den Ende, M.P., Niemeijer, A.R., Spiers, C.J., 2019. Influence of grain boundary structural evolution on pressure solution creep rates. J. Geophys. Res.: Solid Earth 124 (10), 10210–10230. https://doi.org/10.1029/2019JB017500.
Veveakis, M., Poulet, T., 2020. A note on the instability and pattern formation of shrinkage cracks in viscoplastic soils. Geomech. Energy Environ. https://doi.org/10.1016/j.gete.2020.100198.
Veveakis, E., Regenauer-lieb, K., 2015. Cnoidal waves in solids. J. Mech. Phys. Solids 78 (September 2009), 231–248. https://doi.org/10.1016/j.jmps.2015.02.010.
Veveakis, E., Poulet, T., Alevizos, S., 2014. Thermo-poro-mechanics of chemically active creeping faults. 1: Theory and steady state considerations. J. Geophys. Res.: Solid Earth 119 (6), 4583–4605. https://doi.org/10.1002/2013JB010071.
Wang, Y., Chen, L.Q., Khachaturyan, A.G., 1993. Kinetics of strain-induced morphological transformation in cubic alloys with a miscibility gap. Acta Metallurgica Et Materialia 41 (1), 279–296. https://doi.org/10.1016/0956-7151(93)90359-Z.

Weyl, P.K., 1959. Pressure solution and the force of crystallization: a phenomenological theory. J. Geophys. Res. 64 (11), 2001–2025. https://doi.org/10.1029/JZ064i011p02001.

Xu, Z., Meakin, P., 2008. Phase-field modeling of solute precipitation and dissolution Phase-field modeling of solute precipitation and dissolution 014705. https://doi.org/10.1063/1.2948949.

Zhang, L., Steinbach, I., 2012. Phase-field model with finite interface dissipation: extension to multi-component multi-phase alloys. Acta Mater. 60 (6–7), 2702–2710. https://doi.org/10.1016/j.actamat.2012.02.032.

Ziegler, H., 1983. An introduction to thermodynamics. North-Holland.